2022

DEVELOPMENT AND VALIDATION OF A FORCE MEASURING DEVICE FOR A LABORATORY WAVE TANK

Jacob K. Colling
Michigan Technological University, jcolling@mtu.edu

DEVELOPMENT AND VALIDATION OF A FORCE MEASURING DEVICE FOR A LABORATORY WAVE TANK

By

Jacob K. Colling

A REPORT

Submitted in partial fulfillment of the requirements for the degree of

MASTER OF SCIENCE

In Mechanical Engineering

MICHIGAN TECHNOLOGICAL UNIVERSITY

2022

This report has been approved in partial fulfillment of the requirements for the Degree of MASTER OF SCIENCE in Mechanical Engineering.

Department of Mechanical Engineering – Engineering Mechanics

Report Advisor: *Dr. Gordon G. Parker*

Committee Member: *Dr. Wayne W. Weaver*

Committee Member: *Dr. Hassan Masoud*

Department Chair: *Dr. William W. Predebon*

Dedicated in loving memory of my grandmother, Sheila Thornton. We will miss you.

Table of Contents

List of Figures

List of Tables

Acknowledgements

There are many people I'd like to take this opportunity to thank:

My father, Tim, for teaching me what it means to be an engineer.

My mother, Trisha, for always supporting and believing in me.

My advisor, Dr. Gordon Parker, for taking a chance on me as an undergrad and providing me with ample opportunities to learn and grow as an engineer. Your mentorship and friendship throughout my engineering education have been invaluable.

My brother, Connor, for providing me with an example to aspire to.

My sister, Morgan for helping inspire me to dream big.

My grandfather Tom, for teaching me the importance of practical knowledge and wisdom.

My grandfather Ken, who is likely responsible for my father, brother, and myself all becoming engineers.

John and Cathi Drake, whose generosity I have benefited from many times and has had an incalculable impact on my educational journey.

Thank you to these and the many other people in my life who have had a profound positive influence on me. I would not be the person I am today without them.

Definitions

t = time

m = total mass

g = gravitational acceleration

ζ = vertical buoy displacement from the calm water surface to the buoy geometric center

$\dot{\zeta}$ = buoy velocity in the vertical direction

$\ddot{\zeta}$ = buoy acceleration in the vertical direction

F_{PTO} = force exerted on the buoy by the power-take-off

F_{H20} = force exerted on the buoy by the water

$F_{H20_{st}}$ = the hydrostatic force (static component of F_{H20})

$F_{H20_{dy}}$ = the hydrodynamic force (dynamic component of F_{H20})

$F_{FK_{dy}}$ = dynamic Froude-Krylov force

F_D = diffraction force

F_R = radiation force

F_{ex} = excitation force

ρ_{H20} = mass density of water

V_{sub} = submerged buoy volume

r = radius of a spherical buoy

h = buoy depth of submersion

λ = wavelength

T = wave period

d = water depth

n = number of experimental data points

i = time index of a data point

Δt = size of a time step

μ_s = coefficient of static friction

ΔF = measured forces zeroed relative to $\bar{F}_{st}$

F_{meas} = raw force measurements

$\bar{F}_{st}$ = average measured force from a static trial used to define a zero for measured forces

$F_{PTO_{st}}$ = theoretical PTO force for the static trial

η = measured wave height

List of Abbreviations

WEC = Wave Energy Converter

MPC = Model Predictive Control

CFD = Computational Fluid Dynamics

NLFK = Nonlinear Froude-Krylov

PTO = Power Take-Off

MARIN = Maritime Research Institute Netherlands

OWC = Oscillating Water Column

FBD = Free Body Diagram

MTU = Michigan Technological University

CAD = Computer-Aided Design

PSU = Power Supply Unit

PID = Proportional – Integral – Derivative

ABS = Acrylonitrile butadiene styrene

NIST = National Institute of Standards and Technology

ASTM = American Society for Testing and Materials

FFT = Fast Fourier transform

BLDC = Brushless DC (Direct Current)

Abstract

The ability to predict the hydrodynamic force exerted on floating bodies plays a critical role in creating more effective control strategies for wave energy converters (WECs). Developing a test apparatus capable of directly measuring the forces exerted on a floating body subjected to a wavefield provides the means to validate theoretical prediction methods with experimental results and to develop data-based prediction methods for hydrodynamic forces. This report will discuss the development and validation of a device that measures the total vertical force exerted on a test artifact. The device requirements and design are discussed to examine the factors taken into consideration during the device's development. Validation experiments were conducted to verify that the design functioned as intended. Representative experiments were completed to demonstrate how the hydrodynamic force can be obtained experimentally and provide illustrative examples of how these experiments would be conducted using the device.

1 Introduction

1.1 Motivation

The concept of harnessing the power of waves in natural bodies of water to produce renewable energy has been explored for over two centuries and continues to be of significant scientific and commercial interest [1]. This is largely due to the abundance, high energy density, and untapped potential offered by wave power in comparison to other more widely implemented renewable energy sources such as wind and solar [1, 2]. One of the primary challenges preventing wave energy from being implemented at scale is its cost relative to other energy production methods [3]. The development of improved control strategies to maximize the energy extraction of wave energy converters (WECs) has been identified as a key development area for increasing the cost effectiveness and viability of implementing WECs at a commercial scale [4].

Critical to the development of nearly all control strategies is the ability to mathematically model the behavior of the system under consideration with a high level of accuracy and computational efficiency. Control system development typically relies heavily on a mathematical model of the dynamic system to be controlled to predict the system and controller behavior. Advanced optimization-based control strategies such as model predictive control (MPC) use dynamic system models while computing their control inputs, making such models and their accuracy vital to successfully implementing these types of controllers. Models used in this way are said to be "implemented in real-time" and must be reliably solvable within a known amount of time. The model solve time must be significantly shorter than the desired controller update rate in order for real-time implementation of the model to be viable and practical. This makes the computational cost of models used for this purpose of the utmost importance.

Most methods of accurately computing the hydrodynamic force exerted on a point absorber WEC are computationally expensive and impractical for real-time implementation [5, 6]. Computational fluid dynamic (CFD) models are fully nonlinear and are commonly used as a "truth" model and the standard of comparison for model accuracy, but have very high

computational costs [7]. Partially-nonlinear methods are less computationally expensive at the cost of reduced model fidelity [8]. Nonlinear Froude-Krylov (NLFK) force models are a particularly appealing partially-nonlinear method of computing the hydrodynamic forces acting on a point absorber WEC. This is because NLFK models 1) are able to capture the behavior of nonlinearities that significantly affect the behavior of point absorbers and 2) have existing computationally efficient solution methods for common special cases [5, 6, 8, 9]. Having the ability to determine the hydrodynamic forces via experiment offers a means to experimentally validate these computationally efficient solution methods and develop new extremely computationally efficient data-based prediction methods.

1.2 Presented Work

A device designed to directly measure the total force exerted on a test artifact in a laboratory wave tank was developed and validated. Measurement of the force exerted on the test artifact allows for the difficult to compute hydrodynamic force to be determined experimentally. This force component of interest can be isolated from the total measured force by removing the contributions of the easily computed hydrostatic force and inertial force effects. Having the ability to obtain the hydrodynamic force component experimentally produces two primary results: 1) it allows for the experimental validation of analytical methods of computing hydrodynamic forces and 2) it makes the development and validation of data-based methods of predicting hydrodynamic forces possible. These results improve the ability for hydrodynamic force behaviors to be accurately modeled for point absorber WECs with a low enough computational cost to be suitable for implementation as a part of a real-time control system. This will help make the implementation of more advanced energy maximizing WEC control strategies possible.

1.3 Previous Work

An early example of a device designed to measure the forces exerted on a model scale WEC was the “surge-heave-pitch rig” created at the University of Edinburgh in the 1970’s [10]. The device measured the surge (horizontal) and heave (vertical) forces acting on a

cylindrical float using strain gauge transducers and was also capable of exerting external heave and surge forces on the float [10].

More recent research has built upon the basic concepts established by the surge-heave-pitch rig by creating experimental setups capable of both measuring and exerting forces on scale model WECs based on specific full scale design concepts. Experimental studies conducted at Aalborg University during 2013 and 2017 used a load cell mounted in series with a linear actuator to measure the force applied to a scale model of the Wavestar WEC device [11, 12]. The force measurement was used to experimentally determine the wave excitation moment applied to the model scale WEC [11]. The measured force was also used for force feedback control of the linear actuator to minimize undesirable power take-off (PTO) friction effects during device operation [12]. Experiments conducted at Memorial University of Newfoundland in 2014 and 2017 applied a similar approach to mitigating PTO friction and used a load cell to measure the PTO force exerted on scale model WECs that were based on the Wavebob and PowerBuoy design concepts [13, 14].

Other works have expanded WEC force measuring experiments in different directions. Validation testing was conducted on scale models of the Pelamis and Wavebob WEC concepts at Ecole Centrale de Nantes and the Maritime Research Institute Netherlands (MARIN) in 2012 and measured the tension in the mooring lines used to constrain the devices during large scale wave tank tests [15]. The internal force between the float and spar was also measured on the Wavebob model and used by a control strategy to reduce the device's effective PTO friction [15]. A scale model of the Spar-buoy oscillating water column (OWC) style WEC was tested at the University of Plymouth in 2020 and also measured mooring line tensions [16]. A different approach to determining wave excitation force experimentally was used during a study at the University of Hull in 2017, where the pressure exerted on the bottom of a model scale cylindrical point absorber WEC was measured and used to calculate the approximate excitation force [17]. A study done at Dalian University of Technology in 2018 used a "force balance system" to measure the wave force exerted on an array of four cylindrical point absorber style WECs [18]. These works illustrate other ways that force measurements have been used in WEC research.

2 Methods & Materials

2.1 Theoretical Background

A heaving point absorber style WEC harvests wave energy by capturing the relative motion between a buoyant float and a submerged base. The float oscillates due to the forces exerted on it by the incident waves and the power take-off (PTO) of the WEC converts the mechanical energy of the float motion into electricity. A diagram representing the basic design and function of a heaving point absorber WEC is given in Figure 1.

Consider a spherical buoy at the water's surface that is constrained to only move in the vertical (heave) direction by an attached PTO. This system can be used to accurately model the float behavior of a heaving point absorber WEC. A free body diagram (FBD) of this system is given in Figure 2. Applying Newton's second law of motion to the FBD of Figure 2 allows for the system's equation of motion to be derived. The resulting equation of motion is given as equation 1.

$$F_{PTO} + F_{H20} - mg = m\ddot{\zeta} \tag{1}$$

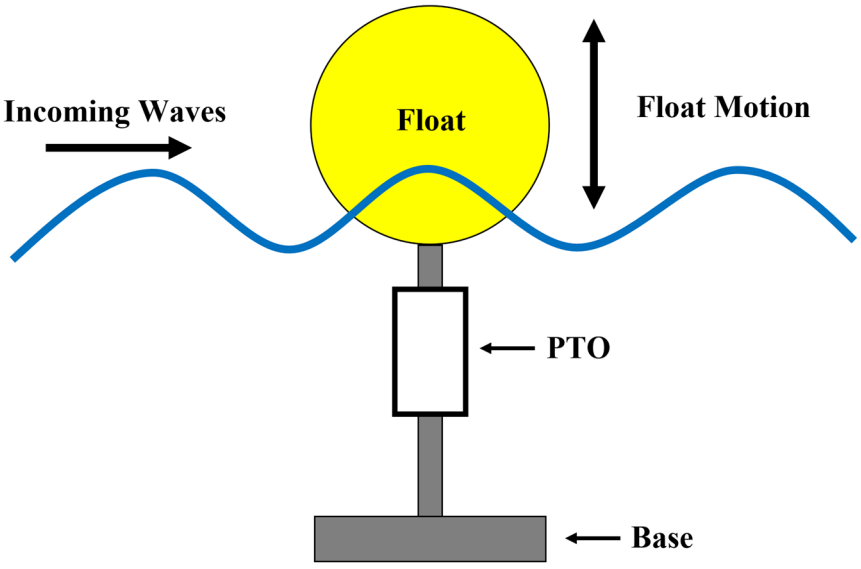

Figure 1: Diagram of a Heaving Point Absorber Style WEC

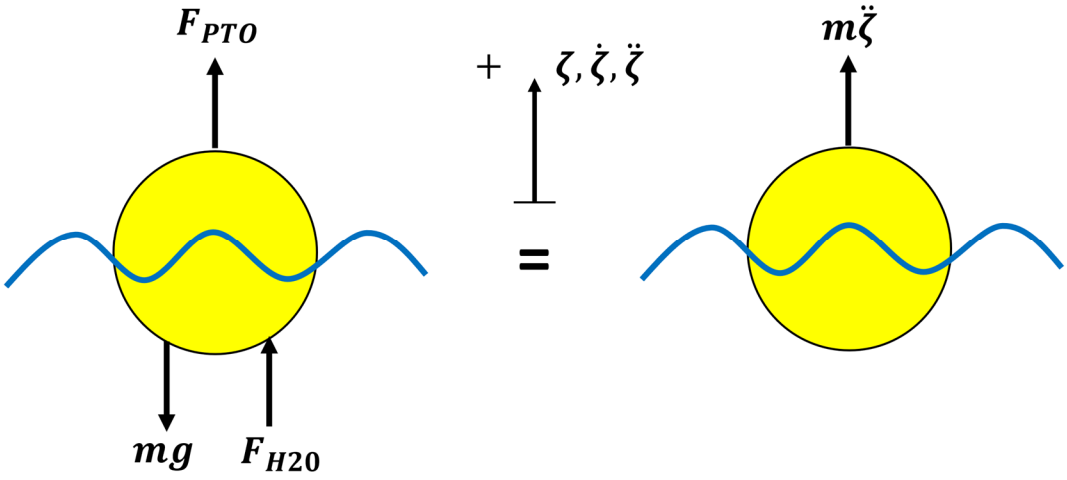

Figure 2: Spherical Buoy Free Body Diagram

F_{PTO} is the force exerted on the buoy by the power-take-off, F_{H20} is the total force exerted on the buoy by the water, m is the total mass, g is gravitational acceleration, ζ is the vertical displacement from the calm water surface to the buoy's geometric center, and $\ddot{\zeta}$ is the buoy's vertical acceleration. F_{H20} can be separated into static ($F_{H20_{st}}$) and dynamic ($F_{H20_{dy}}$) components as shown in equation 2.

$$F_{H20} = F_{H20_{st}} + F_{H20_{dy}} \tag{2}$$

The hydrodynamic force $F_{H20_{dy}}$ can be broken down into multiple components as shown in equation 3.

$$F_{H20_{dy}} = F_{FK_{dy}} + F_D + F_R \tag{3}$$

$F_{FK_{dy}}$ is the dynamic Froude-Krylov force, F_D is the diffraction force, and F_R is the radiation force. These forces result from the undisturbed incident flow potential, diffraction potential, and radiation potential respectively [7]. Equation 3 is formed using potential theory, linear wave theory, and by assuming that the fluid is inviscid and has incompressible and irrotational incident flow [7]. The excitation force F_{ex} is a term that combines the effects of $F_{FK_{dy}}$ and F_D as shown by equation 4 [6]:

$$F_{ex} = F_{FK_{dy}} + F_D \tag{4}$$

Knowledge of F_{ex} is necessary for the implementation of a number of real-time energy extraction maximizing WEC control strategies [17]. This makes the ability to accurately and efficiently predict F_{ex} critical to successfully applying these control approaches. F_{ex} cannot be measured directly for a heaving point absorber WEC, but can be isolated as shown in equation 5:

$$F_{ex} = F_{H20_{dy}} - F_R \tag{5}$$

which allows for F_{ex} to be determined if $F_{H20_{dy}}$ and F_R are known. F_R can found using computationally efficient methods if it is assumed to be linear and is small in magnitude relative to F_{ex} for heaving point absorber WECs operating under controlled conditions [19]. Substituting equation 2 into equation 1 yields an expression that can be solved for $F_{H20_{dy}}$. The resulting equation is given as equation 6.

$$F_{H20_{dy}} = m\ddot{\zeta} + mg - F_{PTO} - F_{H20_{st}} \tag{6}$$

Equation 6 demonstrates how $F_{H20_{dy}}$ can be determined if the PTO force F_{PTO} , hydrostatic force $F_{H20_{st}}$, total mass m, and buoy acceleration $\ddot{\zeta}$ are all known.

F_{PTO} can be measured using a load cell as a part of a force measuring device. $F_{H20_{st}}$ is equal to the weight of the water displaced by the submerged volume of the buoy according to Archimedes' principle and can be calculated as shown in equation 7.

$$F_{H20_{st}} = \rho_{H20} \cdot g \cdot V_{sub} \tag{7}$$

The submerged buoy volume V_{sub} can be determined for a spherical buoy if its radius r and depth of submersion h are known. A diagram showing the relationship between these quantities and ζ is given in Figure 3. The formula for calculating the submerged volume of a spherical buoy is given as equation 8.

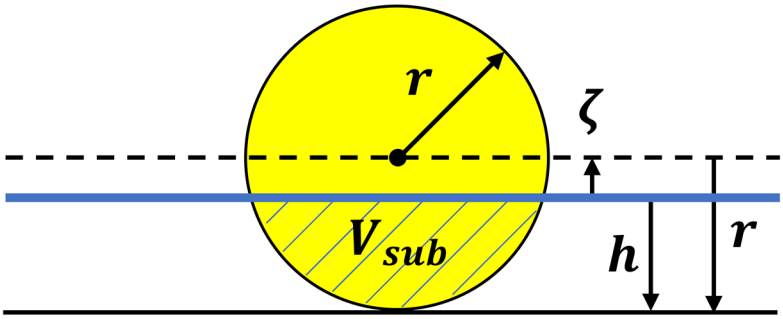

Figure 3: Diagram of a Partially Submerged Spherical Buoy

$$V_{sub} = \begin{cases} \frac{4\pi}{3}r^3 & if \quad h > 2r \\ \frac{\pi h^2}{3}(3r - h) & if \quad 0 \leq h \leq 2r \\ 0 & if \quad h < 0 \end{cases} \tag{8}$$

Note that equation 8 assumes that the depth of buoy submersion is uniform across its diameter. This is only a good assumption when the wavelength of the incident wave is significantly larger than the buoy diameter. The wavelength λ of a wave produced by a wavemaker in water can be found using equation 9 [20]:

$$\lambda = \frac{gT^2}{2\pi}\tanh\left(\frac{2\pi d}{\lambda}\right) \tag{9}$$

where T is the wave period and d is the water depth. The total mass m can be measured directly. The buoy acceleration $\ddot{\zeta}$ can be measured directly or determined from measurements of the buoy position ζ using finite differencing methods. An implementation of these methods for determining $\ddot{\zeta}$ from a series of n measured buoy positions $\zeta_1, \zeta_2, \cdots, \zeta_n$ is given as equation 10 [21]. Note that experimentally acquired position data should be filtered using a low-pass, zero-lag filtering method. This is necessary in order to attenuate the high frequency noise in the data (which is amplified greatly while taking derivatives) and to avoid phase distortion caused by the filtering process [21]. If the position data is ideal (i.e., has no noise) then no filtering is necessary.

$$\ddot{\zeta}_i = \begin{cases} \dfrac{\left(\frac{\zeta_{i+2} - \zeta_i}{2\Delta t}\right) - \left(\frac{\zeta_{i+1} - \zeta_i}{\Delta t}\right)}{\Delta t} & if \quad i = 1 \\ \dfrac{\zeta_{i+1} - 2\zeta_i + \zeta_{i-1}}{\Delta t^2} & if \quad 1 < i < n \\ \dfrac{\left(\frac{\zeta_i - \zeta_{i-1}}{\Delta t}\right) - \left(\frac{\zeta_i - \zeta_{i-2}}{2\Delta t}\right)}{\Delta t} & if \quad i = n \end{cases} \tag{10}$$

2.2 Device Requirements

The device was specifically designed for use in the MTU Wave Tank Laboratory, a picture of which is shown in Figure 4. The MTU wave tank is a 10 m long, 3 m wide, and 1 m deep Edinburgh Designs compact wave flume capable of producing user specified 3D wave profiles. The MTU wave tank has a walkway that spans the width of the tank and is shown in Figure 5. This walkway provides access to areas of the tank that cannot be easily accessed while standing outside of the tank and can be positioned as desired along the length of the tank using its leveling casters.

The primary functions of the presented custom force measuring device are to 1) allow for the placement of a test artifact in the MTU wave tank, 2) provide measurements of the total vertical force exerted on a test artifact, 3) move the test artifact as desired during experiments, and 4) be feasible to construct and practical to use. Design requirements for the device were derived from each of these fundamental device functions.

2.2.1 Device Test Artifact Placement Requirements

The device will be used to place test artifacts at desired locations within the MTU wave tank. The device must be capable of positioning a test artifact at an arbitrary location along the tank length and width. This allows for the test artifact to be subjected to wave fields of interest during experiments and provides the flexibility for the device to accommodate a range of testing configurations. It is highly preferable for the device to not interfere with the operation of the walkway, as this is regularly used and adjusted for experiments.

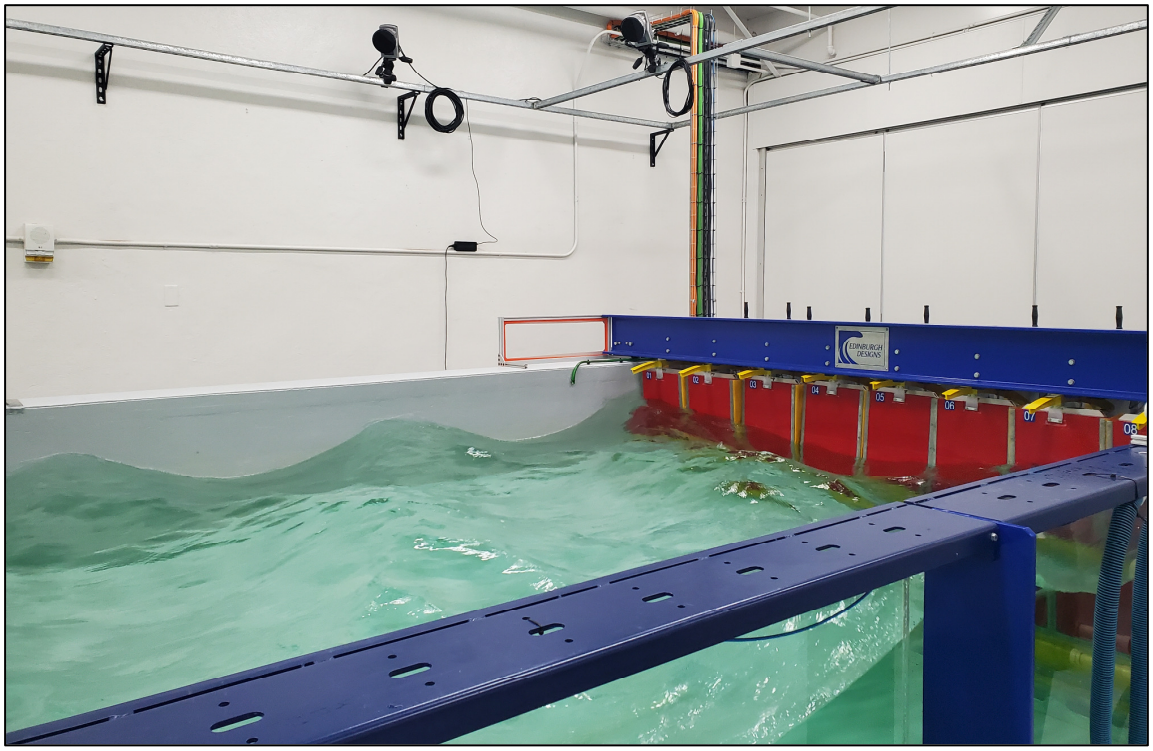

Figure 4: Photograph of the MTU Wave Tank Laboratory

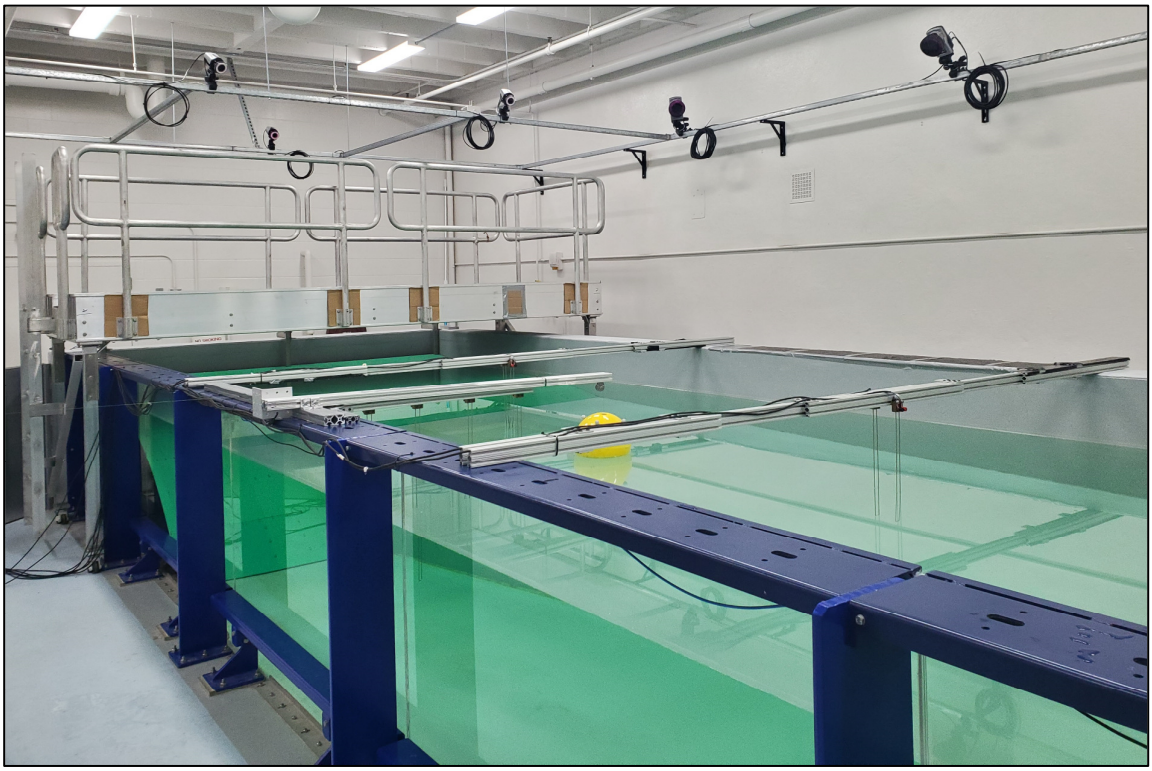

Figure 5: Photograph of MTU Wave Tank with Walkway Shown

2.2.2 Device Force Measurement Requirements

The device must be capable of measuring the total vertical force exerted on a test artifact by the actuator that drives the artifact's motion. This force appears as F_{PTO} in the derived WEC float equation of motion (see *2.1 Theoretical Background*). The device's force measurements must be sufficiently accurate (i.e., the measurements are representative of the true value) and precise (i.e., similar measurement values can be distinguished between) to be of practical value. The device must also be capable of measuring force magnitudes across the full range experienced during the experiments.

2.2.3 Device Test Artifact Motion Requirements

The device must be capable of controlling the vertical position of a test artifact. This allows for the artifact to be positioned as desired with respect to the water surface. The device must be able to move a test artifact to desired static positions and through assigned motion trajectories. This allows for the position, velocity, and acceleration of the test artifact to be controlled during an experiment instead of dictated by the physical attributes of the test artifact and wave field. This is especially important for the experimental validation of mathematical models of hydrodynamic forces. The test artifact motion prescribed by the device must be sufficiently accurate and precise to be useful. The device must also be able to execute a variety of motion trajectories.

2.2.4 Device Feasibility and Practicality Requirements

The device needs to be feasible to create and practical to use to be worth the necessary time and financial investment. This requirement is rather broad in scope, but some of the most important specific considerations are:

1. The benefits provided by the device are worth the required financial investment.
2. The device can be used with a variety of test artifacts (i.e., test artifacts can be swapped out and new ones can be created for new experiments).
3. The device is easily modifiable and configurable.

4. The device can be incorporated into and used in conjunction with existing laboratory instrumentation systems.
5. The device is designed to handle the environmental conditions to which it will be subjected (i.e., the device and its components are water resistant/waterproof).

Fulfillment of these and other practical considerations ensure that the device yields the maximum benefit by providing return on investment, versatility, ease of use, and longevity.

2.3 Device Design

2.3.1 Design Summary

The final design of the force measuring device is presented in Figures 6 and 7, which show the CAD model and assembled device respectively. A system interface diagram showing the connections between the electrical components of the device is given as Figure 8. Further details on the specifics of the device design can be found in Appendix A.

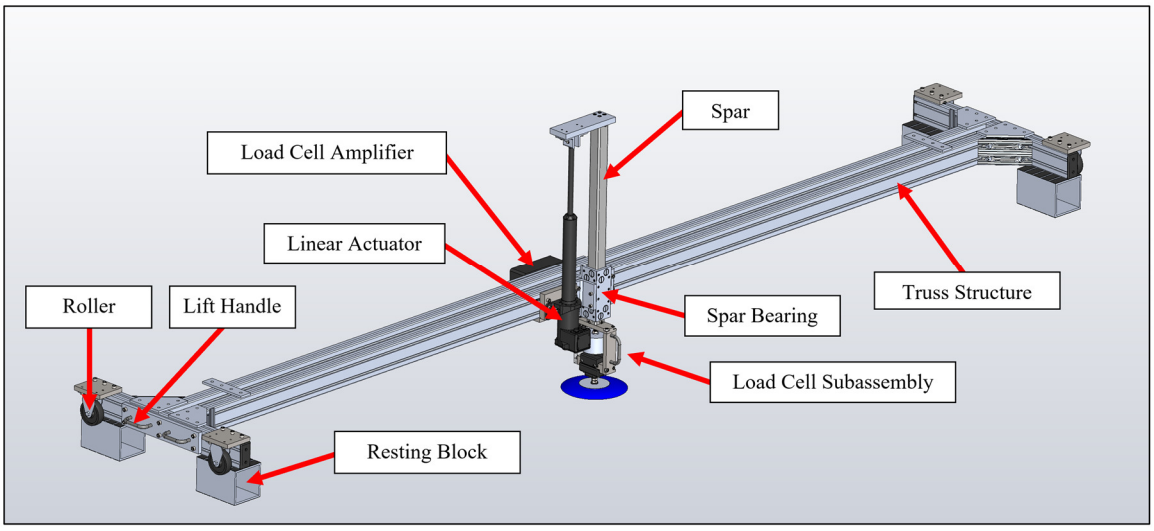

Figure 6: Annotated CAD Model of the Force Measuring Device

The design is mounted on a truss structure constructed out of aluminum extrusion that spans the wave tank. The ends of the truss are fitted with rollers and lift handles to facilitate moving the device into its desired test location. When the device is at its desired test location, it is lifted onto resting blocks to ensure that the device does not move while operating. An Ultra Motion A2 Series electromechanical linear actuator is mounted to the

truss and moves the test artifact in the vertical direction. The actuator is attached to a spar fabricated out of square stainless-steel tube that passes through a large bearing that is mounted directly to the truss. This bearing ensures that the actuator does not experience potentially harmful side loading. A “pancake” style Sensing Systems submersible single axis load cell is contained within a load cell subassembly that is attached to the end of the spar below the spar bearing. The load cell amplifier is attached to an aluminum plate that can be mounted to the truss. The test artifact (a black spherical buoy in the case of this study) is attached using a threaded hole in a shaft at the bottom of the load cell subassembly.

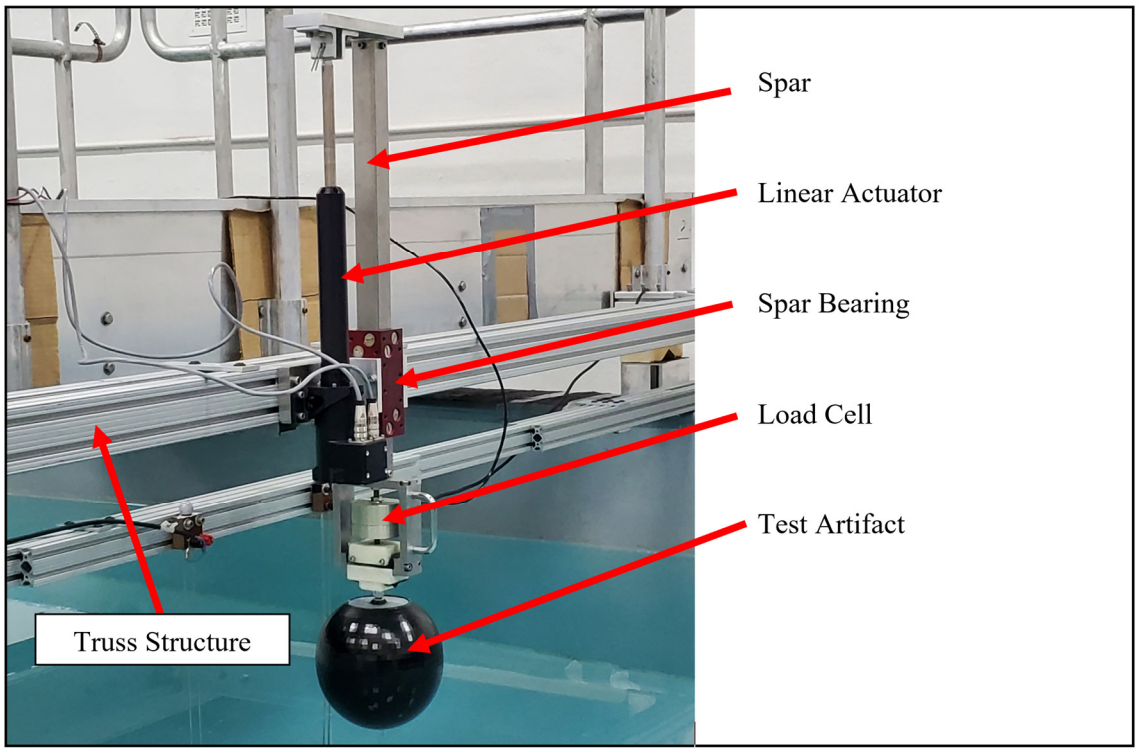

Figure 7: Annotated Photograph of the Force Measuring Device

The device is controlled by a dSPACE MicroLabBox that sends an analog voltage position command to the linear actuator and reads and records the analog voltage signal from the load cell amplifier. The linear actuator is powered by an Ultra Motion PS-1X0A unregulated 180W power supply unit (PSU) that supplies 36 VDC. An emergency stop switch is connected to the PSU to allow for the actuator power to be cut immediately without risk of damaging the system.

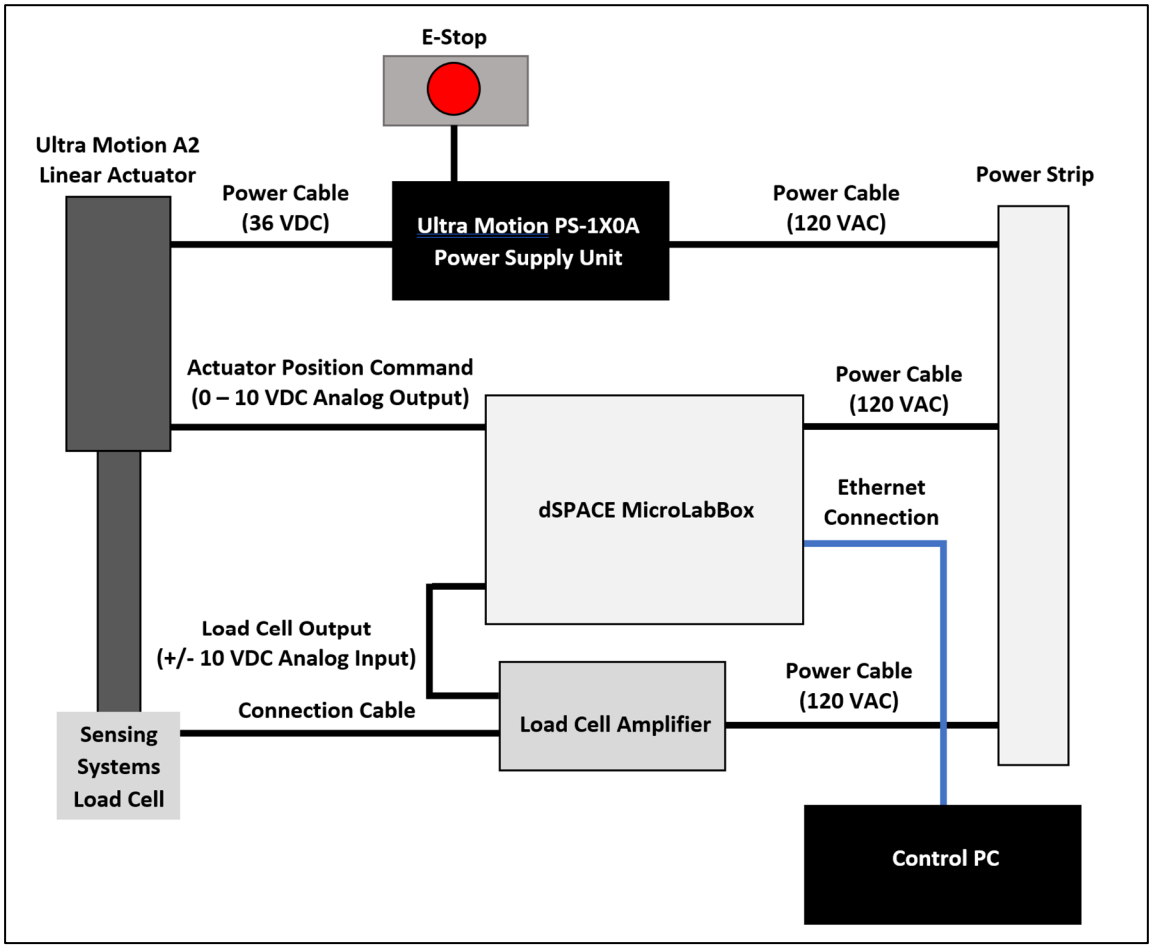

Figure 8: Force Measuring Device System Interface Diagram

The specifics of how the device meets the design requirements discussed in section 2.2 are addressed in subsections 2.3.2 – 2.3.5.

2.3.2 Device Design for Test Artifact Placement

The requirements for test artifact placement dictate that the device allows for a test artifact to be placed arbitrarily within the horizontal plane of the wave tank. This was achieved by 1) having the operating elements of the force device be designed such that they could be attached anywhere along the length of the truss structure that spans the tank and 2) have the truss spanning the tank be designed to allow for it to be rolled on wheels along the length of the tank and be fixed once moved to its desired position. These two features allow for desired artifact placement along the width and length of the tank respectively. The device was also designed such that it can be rolled under the walkway if adjusted from its

operating configuration to a lower profile configuration designed for this purpose. This low-profile configuration is shown in Figure 9 and requires removing the load cell subassembly and the spar from the device and rotating the actuator downwards on a hinge after removing two bolts. Using this configuration of the device allows for the walkway and the force device to move completely independently along the length of the wave tank.

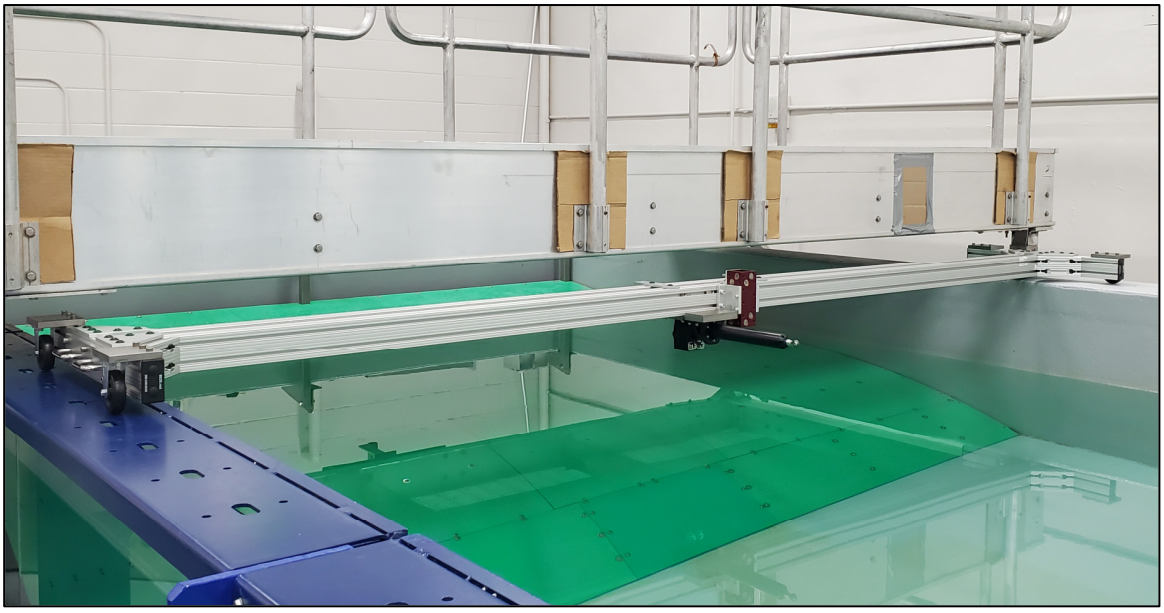

Figure 9: Photograph of the Force Device in the Low-Profile Configuration

2.3.3 Device Design for Force Measurement

A custom Sensing Systems submersible load cell was selected to measure the vertical force exerted by the linear actuator on the test artifact. The load cell has a single measurement axis and a measurement range of +/- 50 lbf (+/- 222 N). The manufacturer specified combined error of the load cell is ≤ 0.250 % of the 50 lbf full scale capacity (i.e., a maximum combined error of +/- 0.125 lbf (+/- 0.556 N)). These measurement capabilities were determined to be appropriate for anticipated future tests in the MTU wave tank. The load cell was mounted below the spar bearing to ensure that the forces were being measured as close to the test artifact as possible to avoid potential measurement distortions.

Side loading of the load cell was an important consideration, as incident waves are expected to apply significant horizontal forces when interacting with the test artifact. Side loading

has the potential to damage the load cell and is generally undesirable. Equivalent side loads can alter force measurements by as much as 3 % of the signal for the selected load cell according to the manufacturer. This source of error is significantly larger than that of the combined error of the load cell itself and therefore presented a major issue. This issue was resolved by mounting the load cell in a subassembly that only transfers forces to the load cell along its measurement axis. This was accomplished by using a linear bearing mounted into an external frame. A shaft that passes through the bearing is mounted to the end of the load cell. This allows for the axial forces to be transferred to the load cell and for the side loads to be absorbed by the bearing and the frame. Figure 10 shows CAD models of the load cell subassembly and the shaft and bearing mechanism.

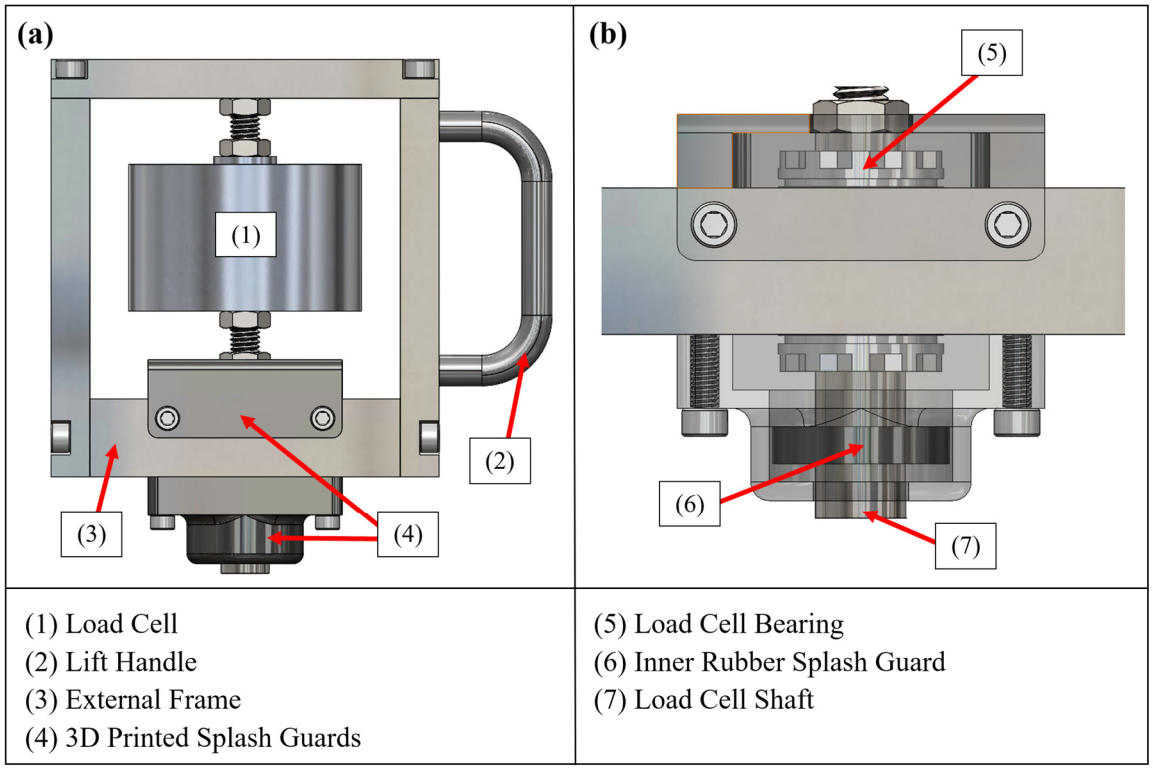

Figure 10: (a) Load Cell Subassembly. (b) Shaft and Bearing Detail View.

The bearing itself introduces a new source of measurement error in the form of friction. The axial force applied through the shaft will be opposed by a friction force with a magnitude equal to the normal force in the bearing multiplied by the bearing static friction coefficient μ_s. The selected load cell bearing (a Thomson SSU10-CR) had a worst-case

static friction coefficient of $\mu_s = 0.004$. This results in a friction force with a magnitude equal to 0.4 % of the applied side load if it is assumed that the normal force within the bearing is equal to the side load applied to the test artifact. This is significantly better than the 3 % error caused by directly side loading the load cell.

2.3.4 Device Design for Test Artifact Motion

Vertical motion of the test artifact was achieved using an Ultra Motion A2 Series industrial electromechanical linear actuator. The base of the actuator was attached to the truss structure with a bracket mount and the end of the actuator shaft was attached to a linkage using a rod bearing clevis and a clevis pin. The linkage was attached to a spar that passed through a bearing and was connected to the load cell subassembly. This was done to ensure that the actuator was not overconstrained or side loaded during device operation. Figure 11 presents annotated images from the device CAD model that show the actuator mounting.

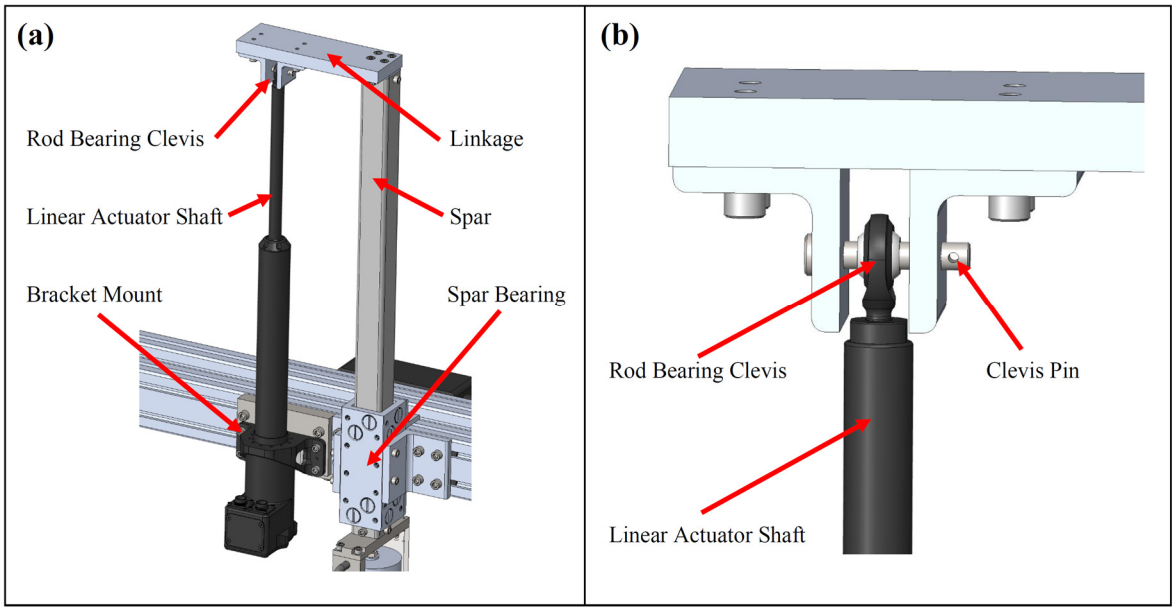

Figure 11: (a) Actuator Mounting Diagram. (b) Linkage Connection Detail View.

The selected actuator had 7.75 in (0.197 m) of actuator travel (stroke) and absolute positioning to a resolution of 122 μin (3.1 μm). This provided the ability to precisely position a test artifact within a wide range of motion. The vertical position of the entire force device could be adjusted by increasing or decreasing the height of the resting blocks

that support the truss structure. This allowed for the vertical distance between the force device and the water surface to be changed, effectively providing a method to adjust the bias of the test artifact's range of motion.

The actuator was rated for a maximum actuator speed of 12.5 in/s (0.318 m/s) under a 50 lbf (222 N) load and a maximum peak force of 180 lbf (801 N) at speeds up to 7.5 in/s (0.1905 m/s) when powered by 36 VDC. The actuator can accept position commands in a variety of formats and uses closed loop PID control to move the actuator to its commanded position. Analog voltage signals proportional to the actuator position were used to command the actuator to execute desired test artifact motion trajectories.

2.3.5 Device Design for Feasibility and Practicality

The cost of the device was determined to be reasonable and justifiable. The cost of materials for the device (at the time of manufacture) was approximately $8,340. A detailed breakdown of the cost on a per component basis can be found in Appendix A.3. This figure excludes the cost of the dSPACE MicroLabBox development system and dSPACE ControlDesk software that were used to control the device as implemented in the MTU Wave Tank Laboratory. Different control hardware and software could be used if desired.

The device has numerous features to maximize its versatility and reconfigurability. The device uses a 3/8" – 16 UNC threaded hole at the bottom of the load cell shaft to allow for a variety of test artifacts to be attached to the device. The aluminum extrusion truss structure that the device is mounted to provides the ability to mount new or modified apparatus to the truss with ease using t-slot nuts. The mechanical design of the device makes the installation of different linear actuators to achieve different artifact motion capabilities straightforward and require minimum design modifications. A new load cell with different measuring capabilities and the same form factor can be ordered from the same load cell manufacturer (Sensing Systems) and swapped into the device to allow for the device's force measuring capabilities to be altered as desired. Sensing Systems' offerings of "custom off the shelf" load cells ensures that a wide selection of device force measuring capabilities can be achieved without changing the design of the device's load

cell subassembly. The device's Ultra Motion linear actuator features a variety of operating modes, the ability to accept a wide range of different command input formats and is highly user configurable. This and the fact that the measurement output of the load cell is a simple analog voltage provides a great deal of flexibility in the choice of hardware and software for device operation. This ensures that the device can be easily integrated into and used in conjunction with other laboratory instrumentation systems.

The device uses materials and components that are suitable for its wet operating environment. The custom machined parts used to construct the device were fabricated out of either 6061 aluminum or 303 stainless steel. 18-8 stainless steel, zinc-plated alloy steel, and 316 stainless steel fasteners were used extensively. The linear actuator is dust and water resistant to the level of an IP65 environmental protection rating. The spar is constructed out of 304 stainless steel and its bearing uses Frelon plastic bearing pads, 316 stainless steel bearing plugs, and an aluminum frame. The load cell is waterproof and can operate while submerged under up to 10 ft (3.048 m) of water. The load cell shaft is constructed out of 440C stainless steel and its bearing uses 440C stainless steel balls and hard chrome-plated bearing plates. Additional protection of the load cell bearing is provided by custom 3D printed splash guards, detailed views of which can be seen in Figure 10.

2.4 Experimental Procedure

The experiments conducted can be categorized as "validation experiments" and "hydrodynamic force determining experiments." The validation experiments were conducted to evaluate how well the force device performed its essential functions. These serve the purpose of validating the device by providing experimental evidence that the device works as intended. The hydrodynamic force determining experiments demonstrate how the device could be used to determine the hydrodynamic force on a test artifact under realistic test conditions. These provide illustrative examples that can serve as a basis for future work and show that the device serves its intended purpose. Both types of experiments are helpful for identifying device limitations and potential improvement areas.

All experiments for this project utilized a dSPACE MicroLabBox development system for data acquisition and controlling test artifact motion (when applicable). The MicroLabBox was controlled using the dSPACE ControlDesk software package, which allowed for purpose-built MATLAB Simulink models to be run on the machine. Force data was acquired by measuring and recording a +/- 10 VDC analog signal that corresponded to the measured force. Measured force was related to the voltage output of the load cell amplifier by a gain of 5 lbf/V. Positive voltages corresponded to the load cell under tension and negative voltages corresponded to the load cell under compression. The position of the linear actuator was controlled with a 0 - 10 VDC analog output, with 0 VDC corresponding to a fully retracted actuator (i.e., the test artifact in its lowest vertical position) and 10 VDC corresponding to a fully extended actuator (i.e., the test artifact in its highest vertical position). A sign convention of positive values acting in the upwards direction was used throughout this project. Actuator commands were user configurable during the experiments and could be recorded along with the force measurement data. Data acquired during the experiments were exported to .mat and .csv file formats for post processing and analysis.

A 3D printed spherical buoy was used for the experiments that required a buoy test artifact. Figure 12 shows an image of the buoy test artifact and Table 1 provides the physical characteristics for it, the mounting hardware, and the load cell. Further details on the buoy's design and fabrication can be found in [22].

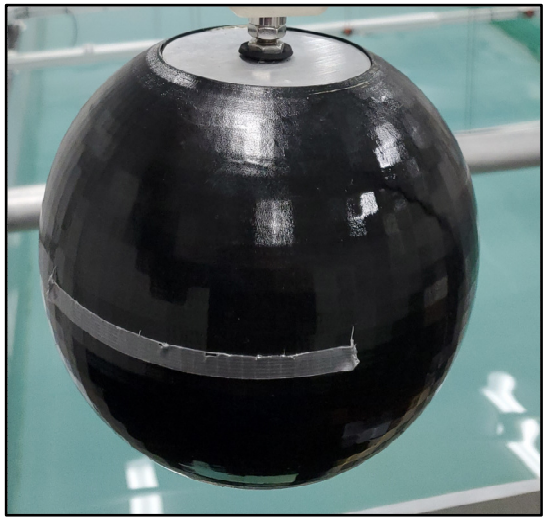

Figure 12: 3D Printed Spherical Buoy Test Artifact

Table 1: Buoy Test Artifact, Mounting Hardware, and Load Cell Physical Characteristics

Physical Characteristic	Value	Units
Buoy Radius r [22]	95.25	mm
Buoy Material [22]	Waterproofed ABS	N/A
Mass of Buoy and Mounting Hardware	0.707	kg
Mass of Load Cell Shaft and Mounting Hardware	0.116	kg
Mass of Load Cell	0.502	kg
Total Mass m	1.325	kg

It is important to note that the orientation of the load cell affects what must be considered as a part of the total mass m. The load cell was mounted in the load cell subassembly "boss side up" (i.e., as shown in Figure 10a where the load cell surface with the small boss face is oriented to be the top surface) during the experiments conducted for this project. In this orientation the mass of the load cell itself must be included in the value of m, as the load cell is measuring its own weight. If the load cell is oriented "boss side down" (i.e., with the small boss face on the bottom load cell surface) then the load cell is not measuring its own weight and the load cell mass should not be included in m.

Note that this section of the report only provides details on the experimental procedures used and does not include a discussion of the post processing of the collected data. The details of the data processing can be found in section 2.5 of this report.

2.4.1 Validation Experiments

These experiments were conducted to validate the primary functions of the device, namely that the device could accurately measure vertical forces and that these measured forces were insensitive to side loading. An experiment was also conducted to evaluate how well the inertial force effects from test artifact motion could be determined from the buoy position command and total mass m.

2.4.1.1 Static Load Experiment

An experiment was conducted to validate the accuracy of the forces measured by the load cell when the load cell is mounted into the load cell subassembly of the device. The load cell itself came from the manufacturer with a NIST traceable force measurement calibration in accordance with the ASTM E4 standard. This experiment was done primarily as a "sanity check" to verify that the device was set up and operating correctly and to provide evidence that the friction of the load cell bearing did not significantly distort the force measurements made by the device. This was not intended to be an in-depth evaluation of the load cell's accuracy and precision, as these goals were already accomplished by the certified calibration performed by the load cell manufacturer.

This experiment was conducted by mounting objects of known weight to the end of the load cell shaft and recording the load cell amplifier output for approximately 10 seconds at a frequency of 128 Hz. These measured force values (which are measurements of the weights of the mounted objects) were then compared to the known object weights to determine the difference between the expected and measured force values. Figure 13 shows an annotated image of the testing setup used to conduct these experiments.

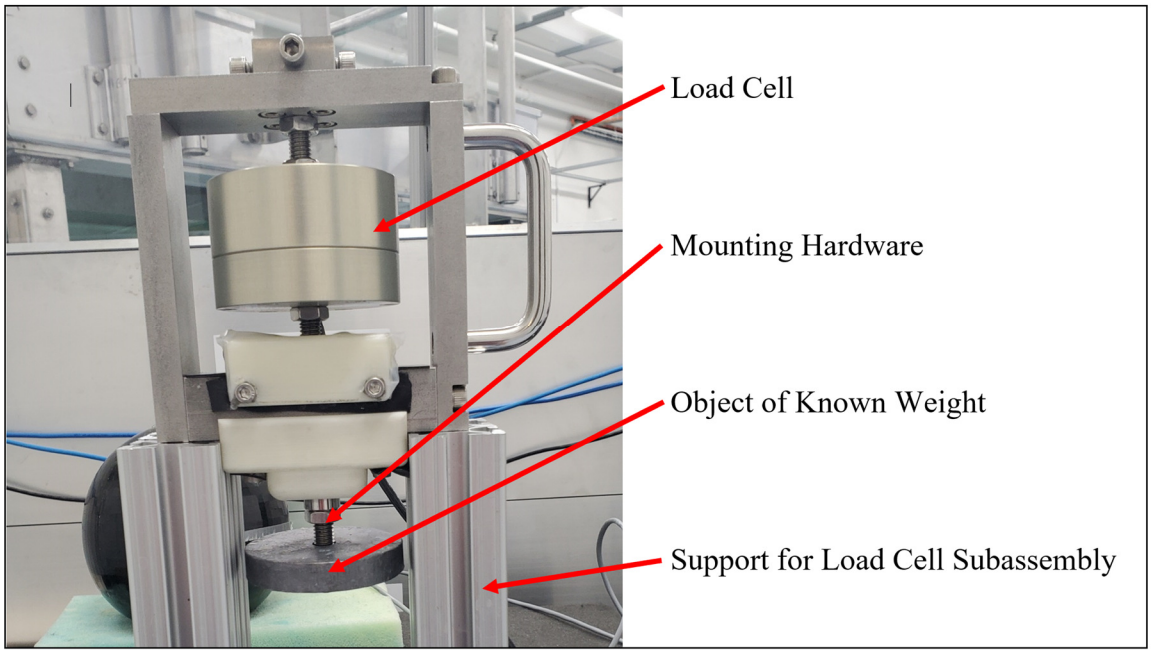

Figure 13: Static Load Experiment Testing Setup

The “known” (i.e., “expected”) weights of the objects were determined by using a digital scale to get the mass of the object to the nearest gram and then multiplying this quantity by gravitational acceleration to get the object’s weight. Experimental trials were conducted with the load cell unloaded (i.e., with only the load cell shaft attached), only the mounting hardware attached, a single weighted disk attached, and two weighted disks attached. The results of this experiment and related discussion are provided in section 3.1.1 of this report.

2.4.1.2 Side Loading Experiments

Experiments were conducted to evaluate the sensitivity of the device force measurements to loads applied perpendicular to the force measurement direction (i.e., side loads). As discussed in section 2.3.3 of this report, side loads and their associated moments have the potential to significantly distort the load cell measurements. The load cell subassembly uses a linear bearing and shaft to prevent side loads from being transferred to the load cell. The primary purpose of this experiment was to investigate the effectiveness of this design.

This experiment was conducted with the load cell subassembly laid on its side (i.e., with its measurement axis perpendicular to the direction of gravity) and by mounting objects of known weight to the end of the load cell shaft. Experimental trials were performed with the objects mounted as close as possible to the end of the shaft and with the objects mounted further away to apply a larger side moment. These trials were designed to test the effects of a pure side load and a combined side load and moment respectively. Figures 14 and 15 show annotated images of the testing setups for the pure side load tests and the combined side load and moment tests respectively. The load cell amplifier output was recorded for approximately 10 seconds at a frequency of 128 Hz for each experimental trial.

Experimental trials for both the pure side load and combined side load and moment experiments were conducted with the load cell unloaded (i.e., with only the load cell shaft and experiment specific mounting hardware attached), a single weighted disk attached, and two weighted disks attached. The results and discussion of these experiments are provided in section 3.1.2 of this report.

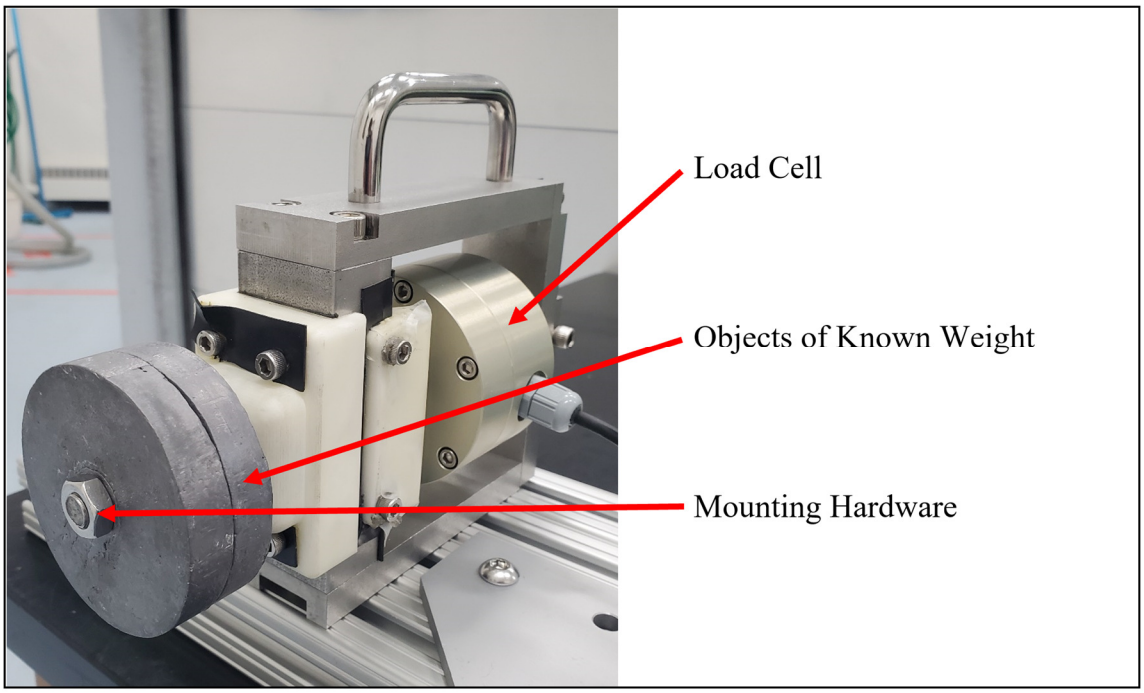

Figure 14: Pure Side Load Experiment Testing Setup

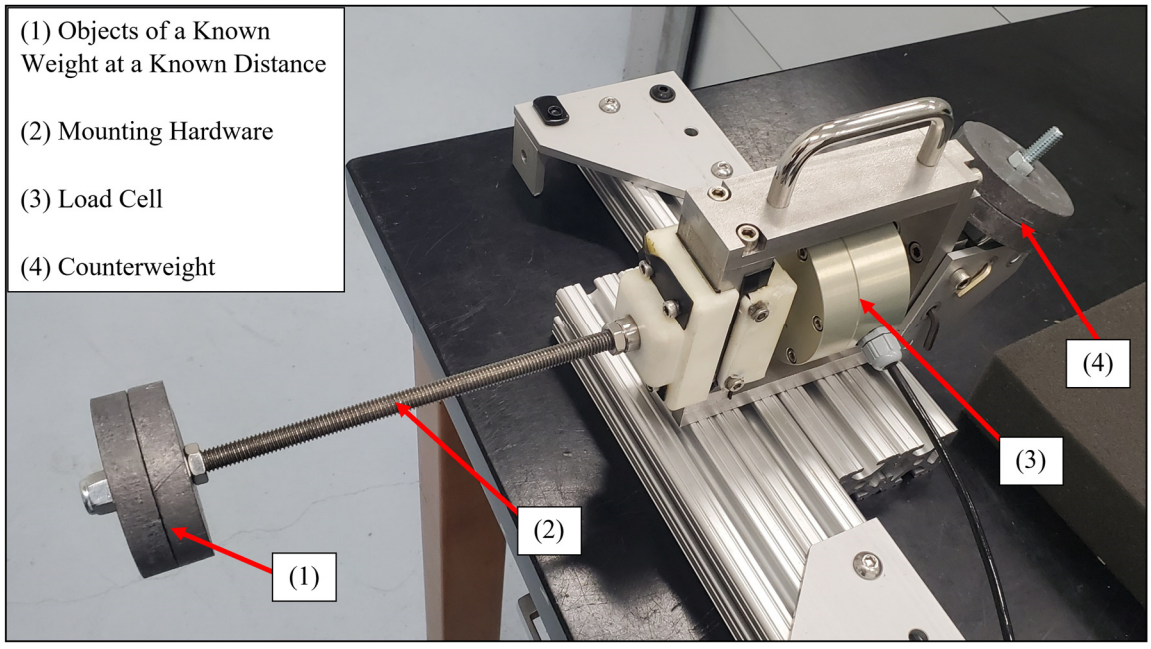

Figure 15: Combined Side Load and Moment Experiment Testing Setup

2.4.1.3 Inertial Force Effects Experiment

An experiment was conducted to evaluate how effectively the inertial force effects caused by the test artifact motion could be determined using knowledge of the actuator position commands and the total mass m. This capability is of interest due to the $m\ddot{\zeta}$ term that appears in the equation for calculating the total hydrodynamic force (see equation 6). This term represents the inertial force effects and can be calculated if the mass and acceleration of the rigid body formed by the test artifact, load cell shaft, load cell (for the load cell orientation used during this study, refer to the relevant discussion in section 2.4 for additional discussion and details), and mounting hardware (i.e., everything mounted to the bottom of the load cell) are known. Mass can be determined by the direct measurement of weight and acceleration can be calculated from position using finite difference differentiation as shown in equation 10. The position command sent to the actuator can be used instead of measured position if it is assumed that the actuator controller has perfect tracking. Determining if this approach is accurate enough to be of practical value was the primary goal of this experiment.

This experiment was conducted with the force device installed in the MTU wave tank and with the spherical buoy test artifact (shown in Figure 12) attached to the device. Additional resting blocks were used to raise the force device higher above the surface of the water to allow for the test artifact to move through an 80 mm range of motion without touching the water. This was done to ensure that experimental trials could be conducted where the measured forces were exclusively the result of the weight of the total mass m and the inertial force effects caused by the mass's acceleration. An annotated image of the testing setup for this experiment is given as Figure 16.

Experimental trials were conducted by moving the test artifact through single frequency sinusoidal motions using the linear actuator. The commanded motion of the test artifact was centered at the middle of the 80 mm range within which the test artifact was not touching the water. This was done to maximize the motion amplitudes that could be realized by the device for this experiment. A static experimental trial with no test artifact motion was conducted to obtain the force measurement that corresponded to only the

weight of the total mass m. Five additional trials were conducted with motion amplitudes between 10 and 40 mm and frequencies between 0.5 and 1.5 Hz. The actuator position command and measured force data were recorded at 100 Hz for approximately 15 seconds during the static trial and approximately 30 seconds during all other trials. The results and discussion of this experiment are provided in section 3.1.3 of this report.

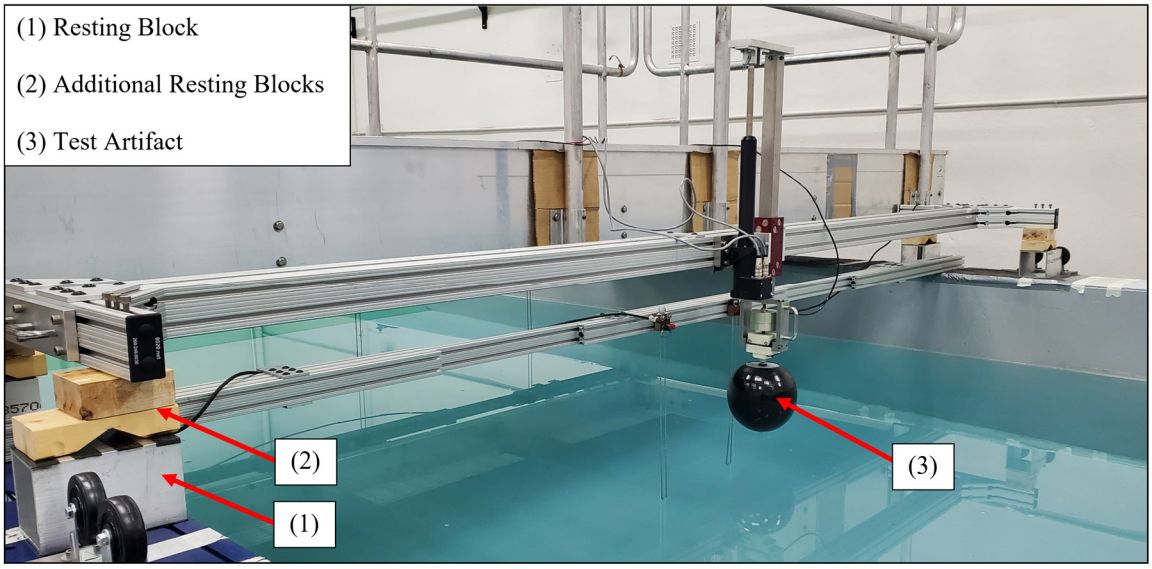

Figure 16: Inertial Force Effects Experiment Testing Setup

2.4.2 Hydrodynamic Force Determination Experiments

These experiments were conducted to demonstrate how the force measuring device can obtain the hydrodynamic force exerted on a test artifact using experimental methods. The specifics of this method were derived in section 2.1 of this report and the equation for calculating the hydrodynamic force using the PTO force measured by the device is given by equation 6. Experiments were performed with a moving test artifact in calm water and a stationary test artifact in a wavefield. These are representative of the types of experiments that could be performed to collect data for validating theoretical methods of calculating the hydrodynamic force and developing data-based hydrodynamic force prediction methods. The primary goals of these experiments were to provide evidence that the device is capable of being used for hydrodynamic force determination, demonstrate how such experiments can be conducted, and identify any potential improvement areas. Both experiments were

conducted with the force device installed in the MTU wave tank and with the spherical buoy test artifact shown in Figure 12.

2.4.2.1 Moving Buoy Experiment in Calm Water

An experiment was conducted to demonstrate how the hydrodynamic force could be determined experimentally for a moving test artifact. Under these test conditions the motion of the test artifact can be prescribed in any manner desired by the researcher (within the limits of the force device's motion capabilities). This allows for specific artifact motions of research interest (such as large amplitude motion of WEC floats) to be explored and specified directly. This experiment considered the simplest case of a moving test artifact in calm water (i.e., water without a wave tank generated wavefield) for demonstration purposes. Providing an illustrative example of a moving test artifact hydrodynamic force determination experiment using the force measuring device was a primary goal of this experiment.

An annotated image of the testing setup for this experiment is given as Figure 17. The actuator position that submerged the buoy to its midline (as shown in Figure 18) was defined as the zero-position for this experiment (i.e., all buoy positions were measured relative to this position). Experimental trials were conducted by moving the buoy through single frequency sinusoidal motions centered about the zero-position. The wave tank was filled to its operating depth of 1 meter prior to the start of the experiment. No waves were generated using the wave tank during any of the experimental trials for this experiment.

A static experimental trial with no buoy motion and the buoy submerged to its midline (i.e., with the buoy at the zero-position) was conducted. The force measurements from the static trial were used to offset the measured forces to be equal to the PTO force (F_{PTO}) as presented in the FBD shown in Figure 2 for all the experimental trials (see *2.5.2 Force Measurement Data Processing*). Fifteen additional trials were conducted with buoy motion amplitudes between 10 and 80 mm and frequencies between 0.25 and 3 Hz. The actuator position command and measured force data were recorded at 100 Hz for approximately 15 seconds during the static trial and approximately 30 seconds during all other trials. The results and discussion of this experiment are provided in section 3.2.1 of this report.

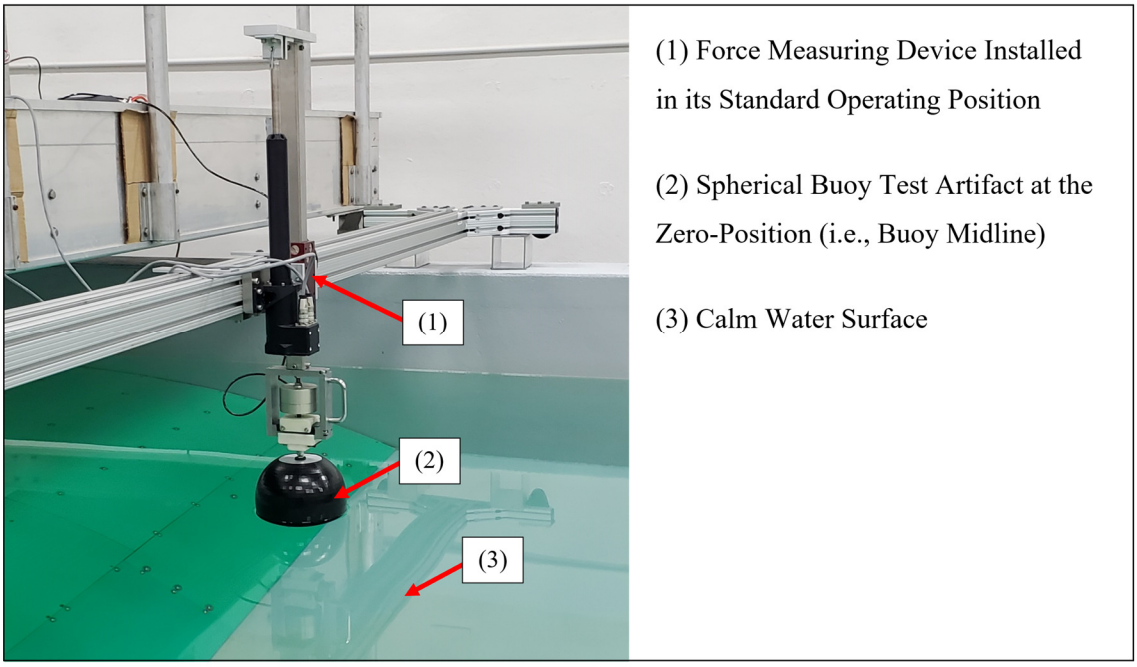

Figure 17: Testing Setup for Moving Buoy Experiment in Calm Water

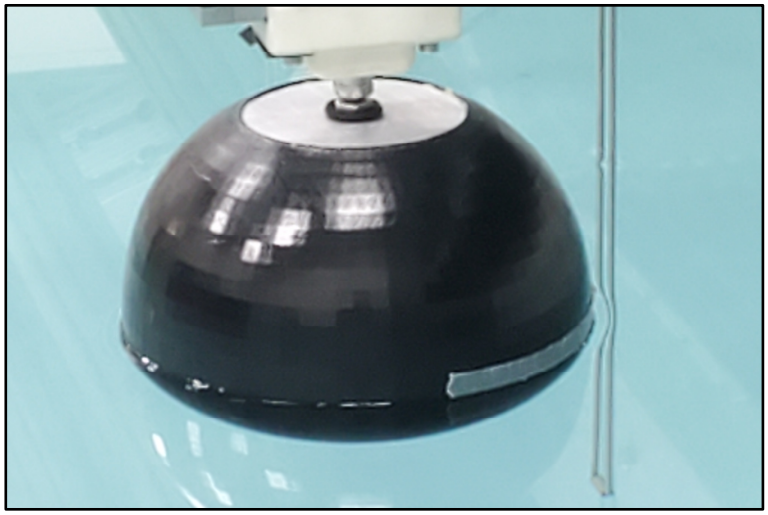

Figure 18: Buoy Zero-Position for Hydrodynamic Force Determination Experiments

2.4.2.2 Stationary Buoy Experiment in a Wavefield

An experiment was conducted to demonstrate how the hydrodynamic force could be determined experimentally for a stationary test artifact in a wavefield. The wavefield is generated by the wave tank, which allows for the wave characteristics to be selected by the researcher. Using a stationary test artifact offers the advantage of knowing the test artifact

acceleration a priori, as it should be exactly zero for all time. It also reduces the number of subcomponents present in the total hydrodynamic force (see equation 3), as the radiation force (F_R) is a function of velocity and zero for a stationary body. This can be beneficial if isolating the excitation force is desired. Providing an example of a stationary test artifact hydrodynamic force determination experiment in a wavefield using the force measuring device was a primary goal of this experiment.

Experimental trials were conducted by holding the buoy stationary at the actuator position that submerged the buoy to its midline (as shown in Figure 18) and using the wave tank to generate single frequency sinusoidal waves that propagated along the length of the tank. An annotated image of the testing setup for this experiment is given as Figure 19. Four Edinburgh Designs resistive wave gauges were used in this experiment to determine the water height. The wave gauges were 0.7 m long and were capable of less than 0.1 % full scale error (i.e., less than 0.7 mm of error) according to the manufacturer. The wave gauges were calibrated and zeroed at the level of the calm water surface after the wave tank had been filled to its operating depth of 1 meter, making the water depth that submerged the buoy to its midline "zero" with respect to wave height. The wave gauges nearest to the buoy were used to determine the water height across the buoy cross section by assuming that the entire buoy was submerged at the same depth. Wave amplitudes and frequencies were selected to ensure that a maximum possible height variation of less than 10 mm was expected across the entire buoy cross section to ensure that this assumption was reasonable. The wave characteristics were also selected to ensure that they could be generated by the wave tank without being "clipped" (i.e., without the wave peaks not being fully realized due to a larger than possible wave amplitude being requested at a given wave frequency). The collection of the wave gauge data was synchronized with that of the force data by electronically triggering the start of the wave gauge data collection at the same time as the start of the force data collection using the dSPACE MicroLabBox.

A static experimental trial with no generated waves was conducted to obtain the force measurements used to offset the measured forces to be equal to the PTO force (F_{PTO}) as presented in the FBD shown in Figure 2 for all the experimental trials (see *2.5.2 Force*

Measurement Data Processing). Four additional trials were conducted with wave amplitudes between 10 and 50 mm and frequencies between 0.4 and 1 Hz. The measured force and wave height data were recorded at 128 Hz for approximately 15 seconds during the static trial and approximately 30 seconds during all other trials. The results and discussion of this experiment are provided in section 3.2.2 of this report.

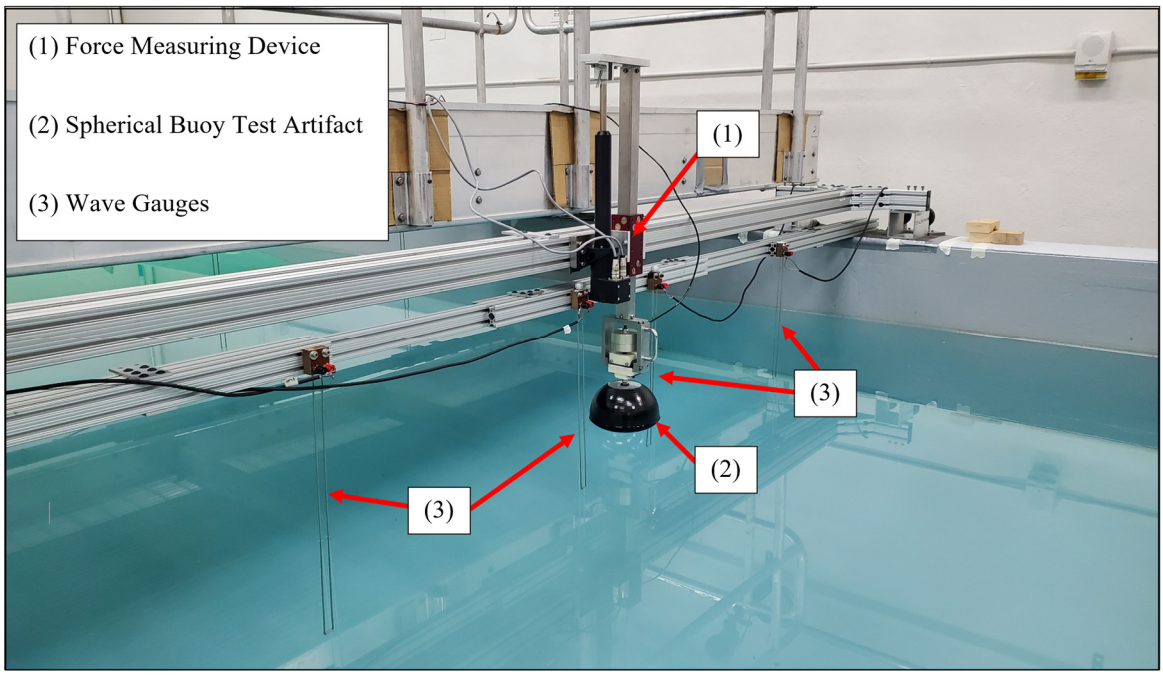

Figure 19: Testing Setup for Stationary Buoy Experiment in a Wavefield

2.5 Data Processing

The experiments performed for this project (which are described in section 2.4) produced three types of recorded data: 1) actuator position commands, 2) force measurements, and 3) wave height measurements. The position commands and force measurements were recorded using the dSPACE MicroLabBox and were exported into .mat and .csv file formats for post processing. The wave height measurements were recorded by the control PC that was connected to the Edinburgh Designs USB Hub in a space delimited .txt file format. The collection of the data using the dSPACE MicroLabBox and Edinburgh Designs USB Hub was synchronized electronically as described in section 2.4.2.2. The raw data

captured during the experiments was processed using MATLAB. The raw experiment data and the MATLAB code used for data processing are provided in Appendix B.

2.5.1 Actuator Position Command Processing

The position command used to control the linear actuator was recorded during the inertial force effects experiment (which is described in section 2.4.1.3) and the moving buoy experiment in calm water (which is described in section 2.4.2.1). The position command is an ideal signal and is not a true measurement. The position command was assumed to be the same as the test artifact position (i.e., it was assumed that the actuator tracked the position command perfectly and that the end effector of the actuator and the test artifact maintained a constant position relative to each other) and was used to estimate the test artifact acceleration during the experiments for which it was recorded.

The position command used for the static trial (a constant value, as the test artifact did not move during this trial) was removed from the position commands of all the trials of a given experiment. This was done to produce position values where zero corresponded to the static trial position of the test artifact. The zeroed position values were then used to find the test artifact acceleration using finite differencing differentiation (see equation 10). No filtering of the position data was necessary due to the positions being derived from an ideal signal without any noise. These calculated accelerations were used to determine the inertial force effects caused by the test artifact motion.

2.5.2 Force Measurement Data Processing

The total force exerted on the test artifact was measured and recorded during all the conducted experiments. The forces measured during the experiments can be separated into two types: static and dynamic. Static forces were measured under unchanging test conditions and should theoretically be constant. They are not constant in practice due to the variations that occur during real physical measurements (e.g., signal noise). The measured static forces were averaged to obtain a single value that was assumed to be constant throughout the duration of the measurement. Dynamic forces were measured under changing test conditions and are expected to change with respect to time. The static

load and side loading validation experiments and the static trials of all the other experiments measured static forces. All other experimental trials measured dynamic forces.

Both static and dynamic forces need to be measured relative to a known zero to be physically meaningful. The zero of the forces measured by the load cell can be configured by hardware adjustments made to the load cell amplifier. However, this is often inconvenient and is only truly necessary in cases where the measured forces span the majority of the load cell's full scale measurement range. A zero can also be set using post processing by subtracting the static force measured during a known set of testing conditions from all the measured forces. This establishes the conditions associated with the measured static force that was subtracted as the zero. This approach provides flexibility in the definition of what the force measurements are being measured relative to. Equation 11 expresses this relationship in terms of the zeroed forces (ΔF), the raw measured forces (F_{meas}), and the average measured static force used to define the new zero ($\bar{F}_{st}$).

$$\Delta F(t) = F_{meas}(t) - \bar{F}_{st} \tag{11}$$

Note that equations 11 – 14 explicitly show time dependencies to more clearly distinguish between time series and scalar variables. The forces measured during the unloaded load cell experimental trials (as defined in the context of each respective experiment) were used to zero the force measurements for the static load and side loading validation experiments. The forces measured during the static trials (as defined in the context of each respective experiment) were used to zero the force measurements for all of the other experiments.

It is desirable to have the measured dynamic forces be expressed relative to a completely unloaded load cell (i.e., a load cell with no force exerted on it). This makes the measured force equal to the PTO force (F_{PTO}) as presented in the FBD shown in Figure 2. This can be accomplished by hardware zeroing the load cell amplifier before the experiments or by using a post processing approach. Consider the buoy shown in the FBD presented in Figure 2 during a static trial when $\dot{\zeta} = \ddot{\zeta} = 0$. Applying Newton's second law of motion under these conditions yields an expression that contains the theoretical PTO force for the static trial, $F_{PTO_{st}}$. An algebraic rearrangement of this expression is given as equation 12.

$$F_{PTO_{st}} = mg - \ F_{H20} \tag{12}$$

Note that during the static trial it is assumed that F_{H20} and V_{sub} are constant and do not change with time. During the static trial it is known that $F_{H20} = F_{H20_{st}}$. Combining this relation with equations 7 and 12 yields equation 13.

$$F_{PTO_{st}} = mg - \ \rho_{H20} \cdot g \cdot V_{sub} \tag{13}$$

It is also known that ΔF is effectively zero for the static trial, as $\bar{F}_{st}$ is the average of the F_{meas} obtained during the static trial. Note that changing the zero about which a measured force is being considered is accomplished by applying a constant offset (as was done by equation 11). Therefore, the offset used to convert ΔF to F_{PTO} for the static trial will be valid for all the experimental trials. An offset of $F_{PTO_{st}}$ converts ΔF to F_{PTO} for the static trial. This reasoning produces equation 14, which can be used to convert the zeroed forces into the desired PTO forces for any trial within a given experiment.

$$F_{PTO}(t) = \Delta F(t) + F_{PTO_{st}} \tag{14}$$

The force offset relations given by equations 11 and 14 were used to convert the measured forces to PTO forces for all the experiments involving dynamic forces.

2.5.3 Wave Height Measurement Processing

The wave height was measured and recorded during the stationary buoy experiment in a wavefield (which is described in section 2.4.2.2). The measured wave heights were used to determine the depth of buoy submersion during this experiment. Wave height data was captured using four wave gauges but only the two wave gauges closest to the buoy were used for the analysis conducted in this report.

The average measured wave height during the static trial was calculated for both wave gauges. These averaged wave heights were used to zero all the wave height measurements by subtracting the average static trial wave height from the measured wave heights for each wave gauge. The zeroed wave heights of the two wave gauges nearest to the buoy were

averaged together at each time step to get an estimate of the average wave height over the submerged cross section of the buoy. The average wave height over the buoy cross-section was calculated using this method for each trial of the stationary buoy experiment.

2.5.4 Hydrodynamic Force Determination

Determining the hydrodynamic force experimentally was a primary purpose of the force measuring device and was done for the hydrodynamic force determination experiments described in section 2.4.2. It is not possible to directly measure the hydrodynamic force, but it can be determined using measured quantities.

Equation 6 demonstrates how the hydrodynamic force ($F_{H20_{dy}}$) can be isolated from the measured PTO force (F_{PTO}) when the total mass (m), buoy acceleration ($\ddot{\zeta}$), and hydrostatic force ($F_{H20_{st}}$) are all known. The process of obtaining the measured PTO force from the raw measured forces is explained in section 2.5.2. The total mass m is given as the last row of Table 1. The buoy acceleration is found from the recorded actuator position commands using the process described in section 2.5.1 if the acceleration is nonzero. The hydrostatic force can be found for a spherical buoy using equations 7 and 8. The depth of buoy submersion h can be found with the buoy position ζ for a moving buoy in calm water using equation 15 if the buoy is submerged to its midline when $\zeta = 0$ and it is assumed that the height of the calm water surface remains constant. The depth of buoy submersion can be found for a stationary buoy in a wavefield with the measured wave height η using equation 16 if the buoy is submerged to its midline when $\eta = 0$ and it is assumed that the depth of submersion is constant across the submerged cross section of the buoy.

$$h = r - \zeta \tag{15}$$

$$h = r + \eta \tag{16}$$

3 Results & Discussion

The results for the experiments described in section 2.4 and associated discussion of the results are given in this section of the report. Details on the analysis used to get these results can be found in sections 2.1 and 2.5.

3.1 Validation Experiments

3.1.1 Static Load Experiment

Table 2 presents the results of the static load experiment. All the reported force values are measured relative to the unloaded experimental trial. The difference was calculated by subtracting the expected force from the measured force.

Table 2: Static Load Experiment Results

Measured Force (N)	Expected Force (N)	Difference (N)
0.629	0.304	0.325
5.844	5.474	0.370
11.085	10.673	0.412

The results presented in Table 2 show that all the differences between the measured and expected forces obtained during this experiment are within the maximum combined error of +/- 0.556 N specified by the load cell manufacturer (see *2.3.3 Device Design for Force Measurement*). These results provide evidence that the load cell was operating correctly and that the friction of the load cell bearing did not meaningfully distort the force measurements made by the device.

3.1.2 Side Loading Experiments

Tables 3 and 4 present the results for the pure side load and the combined side load and moment experiments respectively. All the reported force and moment values are measured relative to the unloaded trial of each experiment. The reported applied moments were considered with respect to the mounting end of the load cell shaft (i.e., the moment arm was measured from the end of the load cell shaft to the center of mass of the added weights).

The 3 % force error was calculated based on the applied side load and is intended to be representative of the force measurement distortion that can occur due to side loading an unprotected load cell (see *2.3.3 Device Design for Force Measurement*).

Table 3: Pure Side Load Experiment Results

Applied Side Load (N)	**Measured Force (N)**	**3 % Force Error**
5.170	-0.0649	0.155
10.369	-0.0796	0.311

Table 4: Combined Side Load and Moment Experiment Results

Applied Side Moment (N-m)	**Applied Side Load (N)**	**Measured Force (N)**
1.07	5.170	-0.0639
2.07	10.369	-0.1204

The results presented in Tables 3 and 4 show that all the measured forces (which are the measured variation from the unloaded trial and should ideally be zero) obtained during this experiment are significantly less than the 3% maximum error that is expected to occur if the load cell were directly side loaded. They are also all well within the maximum combined error of +/- 0.556 N specified by the load cell manufacturer. There appears to potentially be a trend of increasing measured force magnitude with increases in applied side load, but a larger number of experimental trials with larger side loads would need to be conducted to meaningfully explore this relationship.

These results provide evidence that the bearing and shaft design used in the load cell subassembly is effective at limiting the distortion caused to the force measurements by applied side loads and moments. However, the amount of improvement provided by this design over the expected 3 % error for an unprotected load cell cannot be determined with much certainty from these results. This is due to the small magnitude of the obtained force measurements relative to the known maximum load cell error. Additional experimental trials using larger applied side loads should be conducted if a more thorough investigation of this comparison is desired. It is important to note that the load cell subassembly protects the load cell from potential damage caused by side loading in addition to limiting error.

3.1.3 Inertial Force Effects Experiment

Figure 20 presents the first 10 seconds of the results of an experimental trial for a 30 mm amplitude, 1 Hz frequency buoy motion. This trial was selected to be a representative example of the results obtained during this experiment. Plots of the first 10 seconds of the results for all the experimental trials can be found in Appendix C.1.

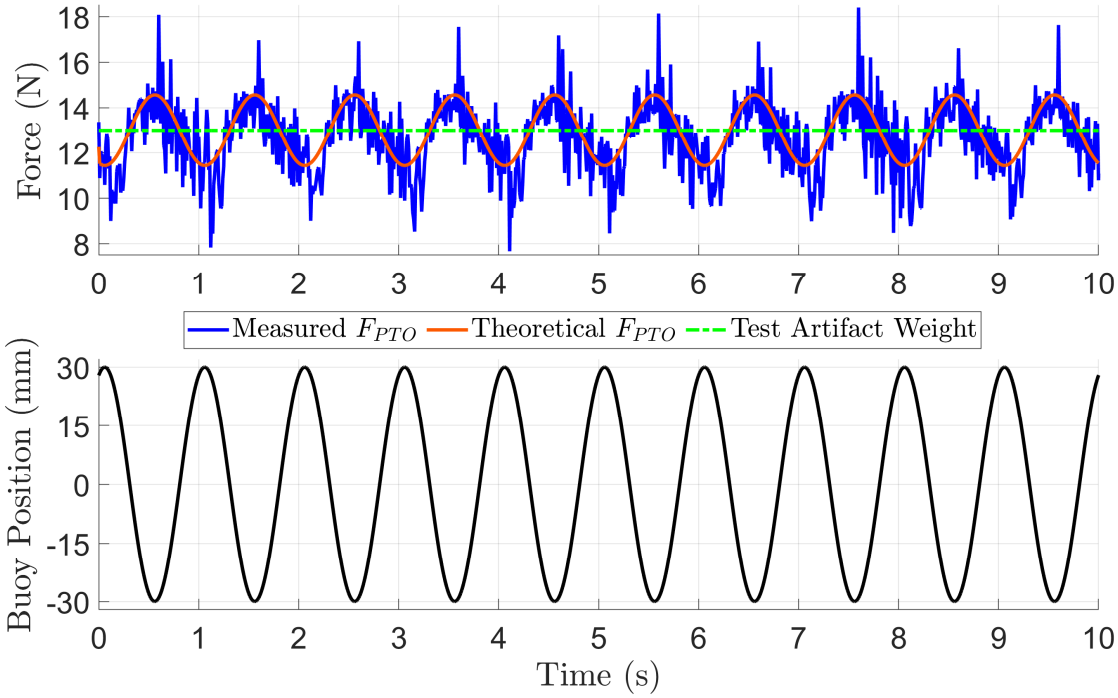

Figure 20: Inertial Force Effects for 30 mm Amplitude 1 Hz Frequency Trial

The theoretical value of F_{PTO} was calculated using an algebraic rearrangement of equation 1. It is known a priori that $F_{H20} = 0$ during this experiment due to the buoy not interacting with the water. This makes F_{PTO} a function of only the buoy acceleration and total mass m. Examining the plot presented in Figure 20 reveals that the measured values of F_{PTO} appear to follow the same pattern as the theoretical values but with a large amount of added noise. The frequency content of the F_{PTO} signal can be further investigated using a Fast Fourier transform (FFT). This analysis can be done using the MATLAB "fft" command and will provide more insight into the nature of the noise in the signal. Figures 21 and 22 present the single-sided amplitude spectrum between 0 and 15 Hz of the measured and

theoretical F_{PTO} signals respectively for the 30 mm amplitude, 1 Hz frequency experimental trial.

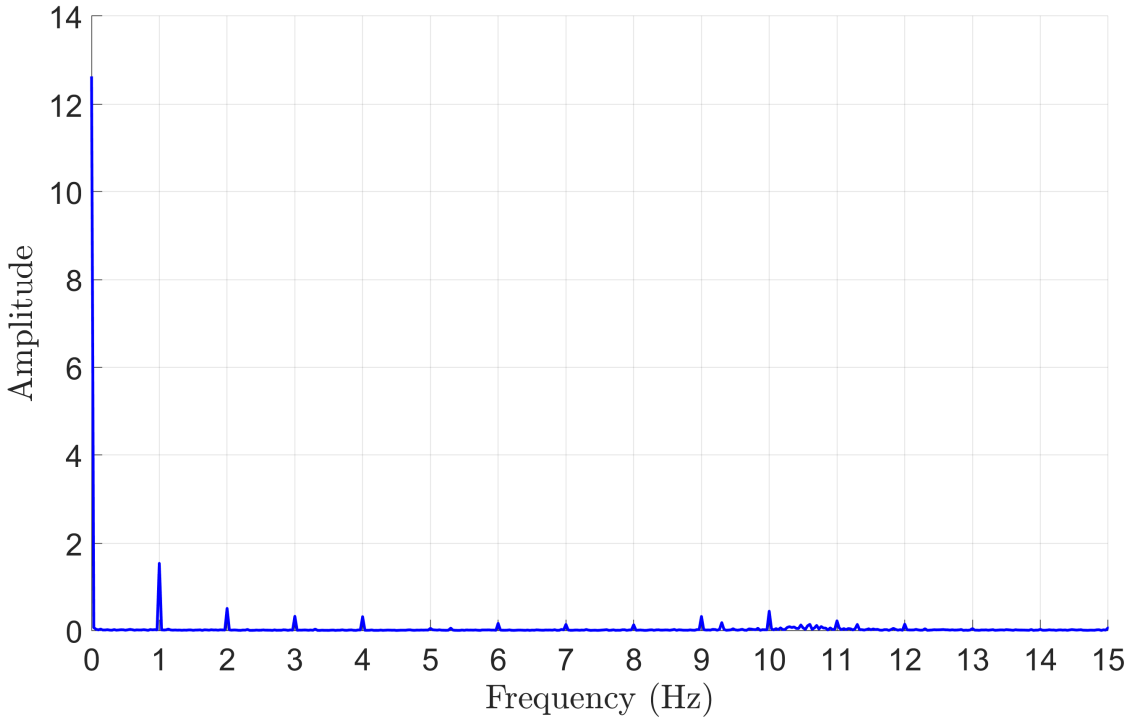

Figure 21: Single-Sided Amplitude Spectrum for Measured PTO Force from Inertial Force Effects 30 mm Amplitude 1 Hz Frequency Trial

Examining Figures 21 and 22 reveals that the largest two amplitudes are at 0 Hz and 1 Hz for both the measured and theoretical PTO forces. This is expected, due to the large DC (i.e., 0 Hz) force component from the weight of the total mass and the regular 1 Hz motion of the buoy. The measured force has notable additional amplitude spikes of 0.3 or higher at 2, 3, 4, 9, and 10 Hz and many smaller spikes under 0.3 in the 5 – 13 Hz range. The highest frequency content in the signal is 1 Hz based on Figure 22, making the lower frequency spikes in Figure 21 the most likely to contain meaningful signal content.

The higher frequency content of the measured force can be attenuated using a low pass filter. A filter cutoff frequency (i.e., the frequency at which the filter causes -3 dB of attenuation) of 5 Hz was selected due to the largest amplitude low frequency spikes in Figure 21 occurring below 5 Hz. Figure 23 presents the results given in Figure 20 after the measured PTO force was filtered using a zero-lag, fourth order Butterworth filter with a 5

Hz cutoff frequency. The filtering was implemented using the MATLAB "filtfilt" command and was applied to all the experimental trials.

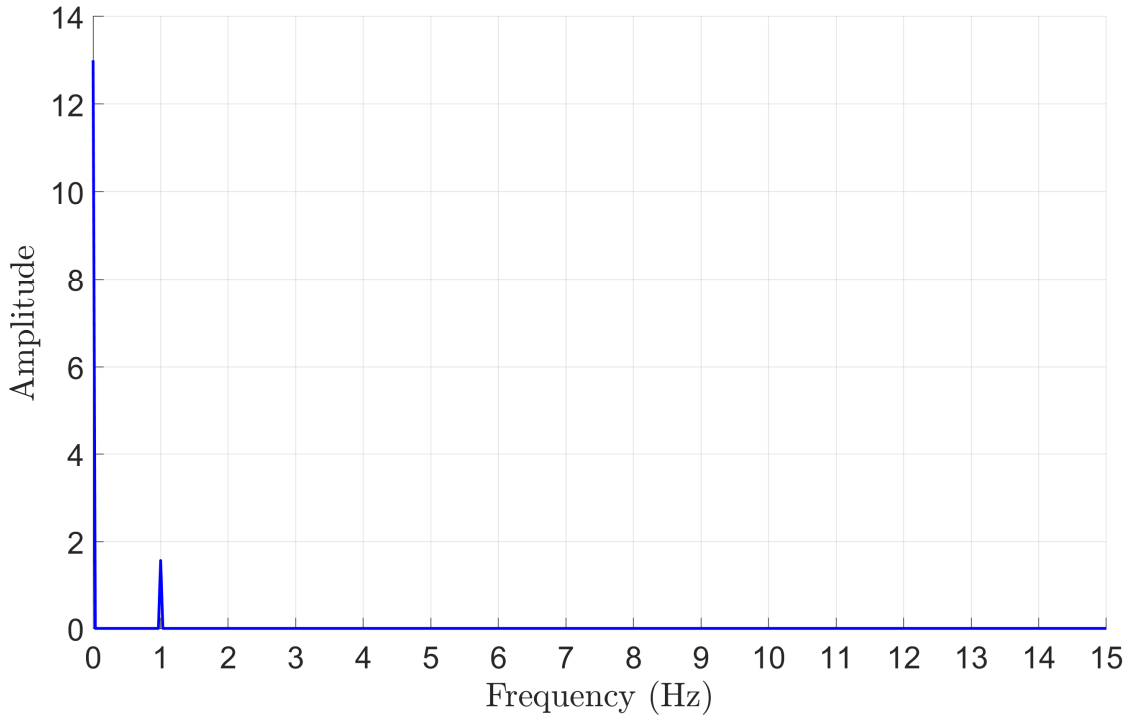

Figure 22: Single-Sided Amplitude Spectrum for Theoretical PTO Force from Inertial Force Effects 30 mm Amplitude 1 Hz Frequency Trial

Comparing Figures 20 and 23 reveals that the measured force data matches much better with the theoretical force values after being filtered but still deviates significantly in some areas. The largest deviations between the theoretical and measured forces in Figure 23 appear to occur right after the buoy reaches its highest vertical position and changes direction. It was observed during the experiment that the truss structure would vibrate, particularly during trials involving higher actuator speeds. This is likely the cause of the unexpected high frequency content (i.e., the noise) in the measured forces. The method used to obtain the buoy acceleration (and therefore the theoretical PTO force) was derived from the actuator position command and assumed completely ideal buoy motion. Consequently, the theoretical PTO force did not take into consideration any non-ideal behavior (such as a vibrating truss), resulting in significant differences between the theoretical and measured PTO forces.

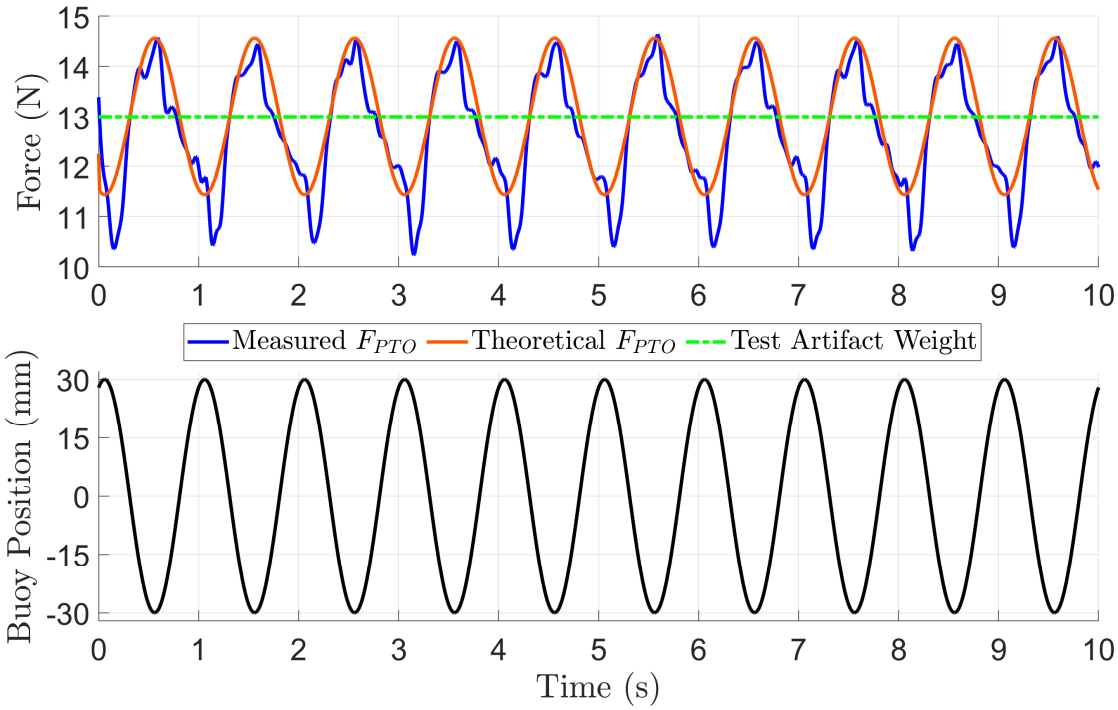

Figure 23: Inertial Force Effects 30 mm Amplitude 1 Hz Frequency Trial with Zero-Phase Filtering Applied to the Measured PTO Force

The magnitude of the difference between the measured and theoretical values of the PTO force was evaluated at each time step for each experimental trial. Tables 5 and 6 present the maximum and average magnitude difference between the measured and theoretical PTO force for each trial for unfiltered and filtered measured force data respectively.

Table 5: Maximum and Average Magnitude Differences Between Unfiltered Measured and Theoretical PTO Forces for the Inertial Force Effects Experiment

Experimental Trial	**Maximum Magnitude Difference (N)**	**Average Magnitude Difference (N)**
Static	0.2510	0.0204
10 mm Amplitude, 1 Hz	2.7130	0.5912
20 mm Amplitude, 1 Hz	3.8266	0.7377
20 mm Amplitude, 1.5 Hz	7.4732	1.4844
30 mm Amplitude, 1 Hz	4.8541	0.9501
40 mm Amplitude, 0.5 Hz	3.9774	0.7740

Comparing Tables 5 and 6 provides quantitative evidence that filtering the measured forces improved the agreement between the measured and theoretical PTO forces across a range

of buoy motions. The tables also show that the magnitude of the differences increase when the amplitude and frequency of the buoy motion increases. This provides evidence that the truss vibration was a contributing factor to the differences between the theoretical and measured force values, as the intensity of truss vibration was observed to increase with increases in buoy motion amplitude and frequency during the experiment. The average magnitude differences of the filtered data are promising, as these values are all within the maximum combined error of the load cell. However, the maximum magnitude differences are much larger and are comparable in size to the inertial force effects.

Table 6: Maximum and Average Magnitude Differences Between Filtered Measured and Theoretical PTO Forces for the Inertial Force Effects Experiment

Experimental Trial	**Maximum Magnitude Difference (N)**	**Average Magnitude Difference (N)**
Static	0.0383	0.0103
10 mm Amplitude, 1 Hz	0.6643	0.3151
20 mm Amplitude, 1 Hz	2.3962	0.3173
20 mm Amplitude, 1.5 Hz	3.7166	0.3006
30 mm Amplitude, 1 Hz	3.9649	0.4593
40 mm Amplitude, 0.5 Hz	1.3943	0.4131

During this experiment the measured forces are only the result of the weight of the total mass and the inertial force effects caused by the buoy's motion. This allows for the results of this experiment to be used to evaluate the effectiveness of using the actuator position command and measured total mass to calculate the inertial force effects of a moving test artifact. The results of this experiment indicate that there is a significant difference between the theoretical and measured PTO force when applying this method (i.e., that there is significant error associated with this method). Reducing the noise in the measured force by eliminating or reducing truss vibration and using a more effective method of obtaining the test artifact acceleration are necessary to improve the performance of this method.

3.2 Hydrodynamic Force Determination Experiments

3.2.1 Moving Buoy Experiment in Calm Water

Figure 24 presents the first 10 seconds of the results of an experimental trial for a 50 mm amplitude, 1 Hz frequency buoy motion. This trial was selected to be a representative example of the results obtained during this experiment. Plots of the first 10 seconds of the results for all the experimental trials can be found in Appendix C.2.

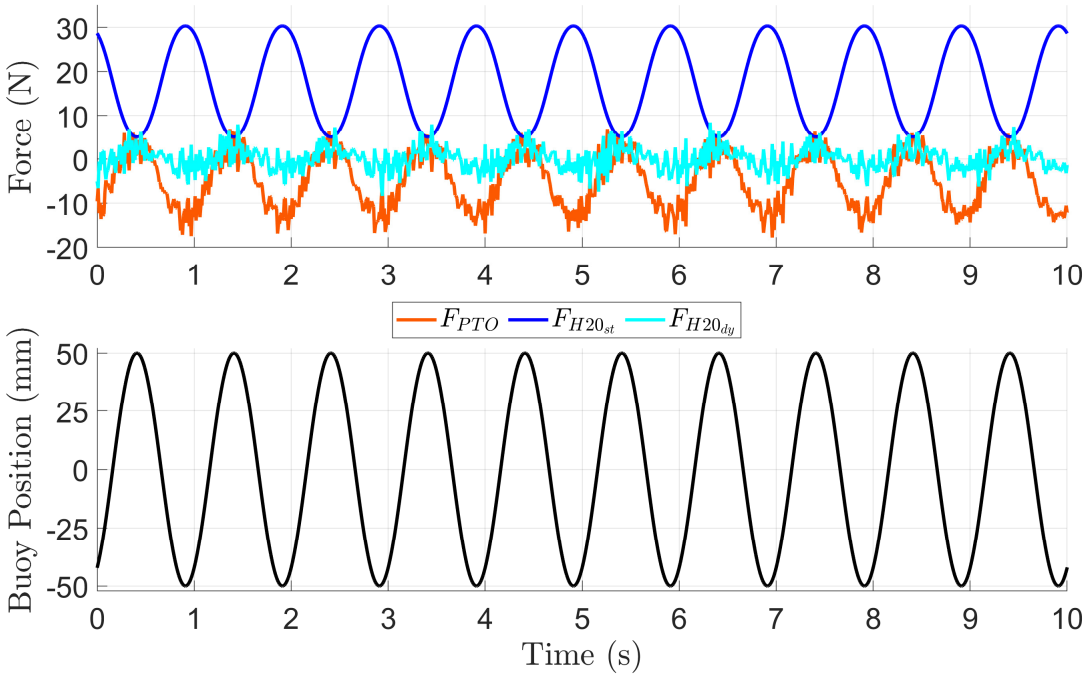

Figure 24: Moving Buoy 50 mm Amplitude 1 Hz Frequency Trial

Figure 24 presents the measured PTO force (F_{PTO}), the hydrostatic force ($F_{H20_{st}}$), and the hydrodynamic force ($F_{H20_{dy}}$). The details on the methods used to determine $F_{H20_{st}}$ and $F_{H20_{dy}}$ can be found in section 2.5.4. Examining Figure 24 reveals that the measured PTO force appears to contain noise like the results presented in Figure 20, although to a lesser degree. The noise can be evaluated and mitigated using an FFT and a zero-lag, fourth order Butterworth filter respectively, as was done for the inertial force effects experiments (see section 3.1.3). Figure 25 presents the single-sided amplitude spectrum between 0 and 15 Hz of the measured F_{PTO} signal for the 50 mm amplitude, 1 Hz frequency trial.

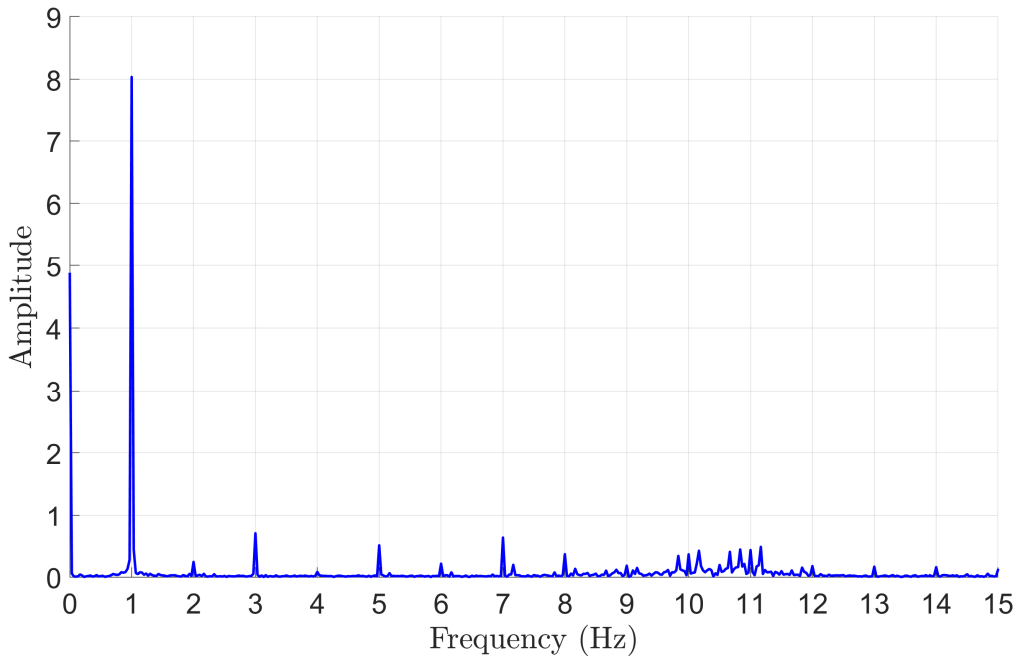

Figure 25: Single-Sided Amplitude Spectrum for Measured PTO Force from Moving Buoy 50 mm Amplitude 1 Hz Frequency Trial

Examining Figure 25 shows large amplitude peaks at 0 and 1 Hz (as expected due to the large DC component of the measured force and 1 Hz motion of the buoy) and numerous smaller peaks at higher frequencies. The spectrum appears comparable to that of Figure 21 (as both have their largest spikes at 0 and 1 Hz) and resulted from a similar type of experiment (i.e., a moving buoy experiment). Therefore, the same cutoff frequency (5 Hz) was used for the moving buoy experiment as was used for the inertia force effects experiment. Figure 26 presents the results given in Figure 24 after the measured PTO force was filtered using a zero-lag, fourth order Butterworth filter with a 5 Hz cutoff frequency.

Comparing Figures 24 and 26 shows that the filtered force data looks much cleaner without causing a significant observable loss in signal amplitude. Examining Figure 26 reveals that the hydrodynamic force is significantly smaller in magnitude than the hydrostatic force and appears to be in phase with the PTO force and buoy position. Investigating the magnitude of the hydrodynamic forces obtained during these experiments provides insight into if these values are large enough to be meaningfully measured by the load cell. The maximum and average hydrodynamic force magnitude was calculated for all the experimental trials after filtering the measured PTO force and are presented in Table 7.

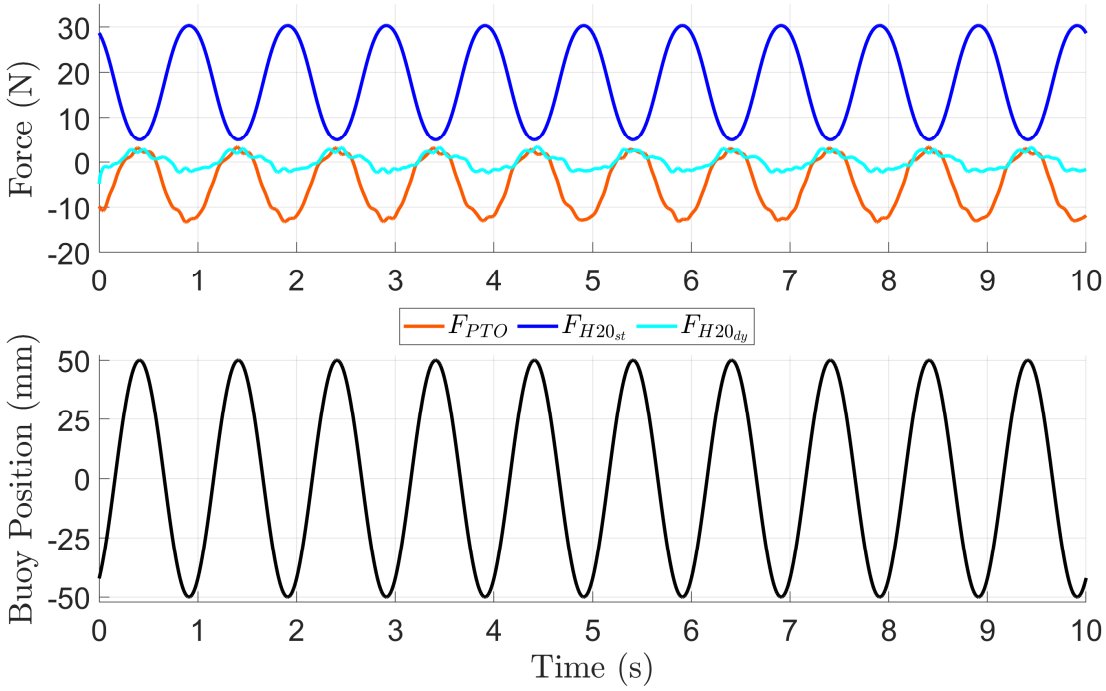

Figure 26: Moving Buoy 50 mm Amplitude 1 Hz Frequency Trial with Zero-Phase Filtering Applied to the Measured PTO Force

Table 7: Maximum and Average Hydrodynamic Force Magnitude from the Filtered Force Results of the Moving Buoy Experiment

Experimental Trial	**Maximum Hydrodynamic Force Magnitude (N)**	**Average Hydrodynamic Force Magnitude (N)**
10 mm Amplitude, 1 Hz	1.216	0.474
10 mm Amplitude, 2 Hz	2.479	0.840
10 mm Amplitude, 3 Hz	4.120	1.980
20 mm Amplitude, 0.5 Hz	1.077	0.510
20 mm Amplitude, 1 Hz	2.724	0.954
20 mm Amplitude, 1.5 Hz	3.069	1.038
20 mm Amplitude, 2 Hz	4.401	1.547
40 mm Amplitude, 0.5 Hz	3.418	1.032
40 mm Amplitude, 1 Hz	4.701	1.496
50 mm Amplitude, 1 Hz	4.857	1.846
50 mm Amplitude, 2 Hz	5.531	2.133
80 mm Amplitude, 0.25 Hz	3.399	0.875
80 mm Amplitude, 0.5 Hz	2.884	1.171
80 mm Amplitude, 0.75 Hz	5.575	1.364

Examining the results presented in Table 7 shows that the maximum and average force magnitudes compare favorably to the +/- 0.556 N maximum combined error of the load cell. All the maximum and average hydrodynamic force magnitudes (except for the 10 mm amplitude, 1 Hz and 20 mm amplitude, 0.5 Hz trial averages) are greater than the maximum combined load cell error. This provides evidence that the determined hydrodynamic forces are caused by a physical phenomenon and are not the result of measurement variation created by error in the load cell. However, these force magnitudes are similar in size to the maximum combined load cell error, limiting the usefulness of these measurements.

This experiment has provided an example of how hydrodynamic force determination could be performed using the force measuring device for a moving test artifact in calm water. The results show promise, producing measured forces that appear less noisy than those of the inertial force effects experiment and hydrodynamic forces of measurable magnitude. However, there are several significant limitations on these results that require scrutiny. A constant water surface height was assumed during the experiment, which is an approximation whose validity requires investigation. The results of the inertial force effects experiments indicated that the method used during the moving buoy experiment to determine the inertial force effects (i.e., the $m\ddot{\zeta}$ term in equation 6) has significant error. These limitations have the potential to produce significant discrepancies between the true and calculated values of the hydrostatic force and inertial force effects which can cause nonexistent force components to appear in the hydrodynamic force. This is a result of the hydrodynamic force being determined using the calculated quantities for the hydrostatic force and inertial force effects as demonstrated by equation 6. These issues, along with the hydrodynamic forces being similar in magnitude to the combined load cell error, would need to be resolved in order to conduct moving buoy experiments capable of producing results that could be used with confidence for further research purposes.

3.2.2 Stationary Buoy Experiment in a Wavefield

Figure 27 presents the first 10 seconds of the results of an experimental trial for a 40 mm amplitude, 0.5 Hz frequency incident wave. This trial was selected to be a representative

example of the results obtained during this experiment. Plots of the first 10 seconds of the results for all the experimental trials can be found in Appendix C.3.

Examining Figure 27 reveals that the measured PTO force appears to be very clean and free of noise for the stationary buoy experiment. This contrasts with the results obtained during the inertial force effects and moving buoy experiments, indicating that test artifact motion is a primary cause of the phenomena that produce the noise in the measured forces during those experiments. The figure also shows that the hydrodynamic force is much smaller than the hydrostatic force, approximately in phase with the measured PTO force, and approximately 180 degrees out of phase with the hydrostatic force and wave height.

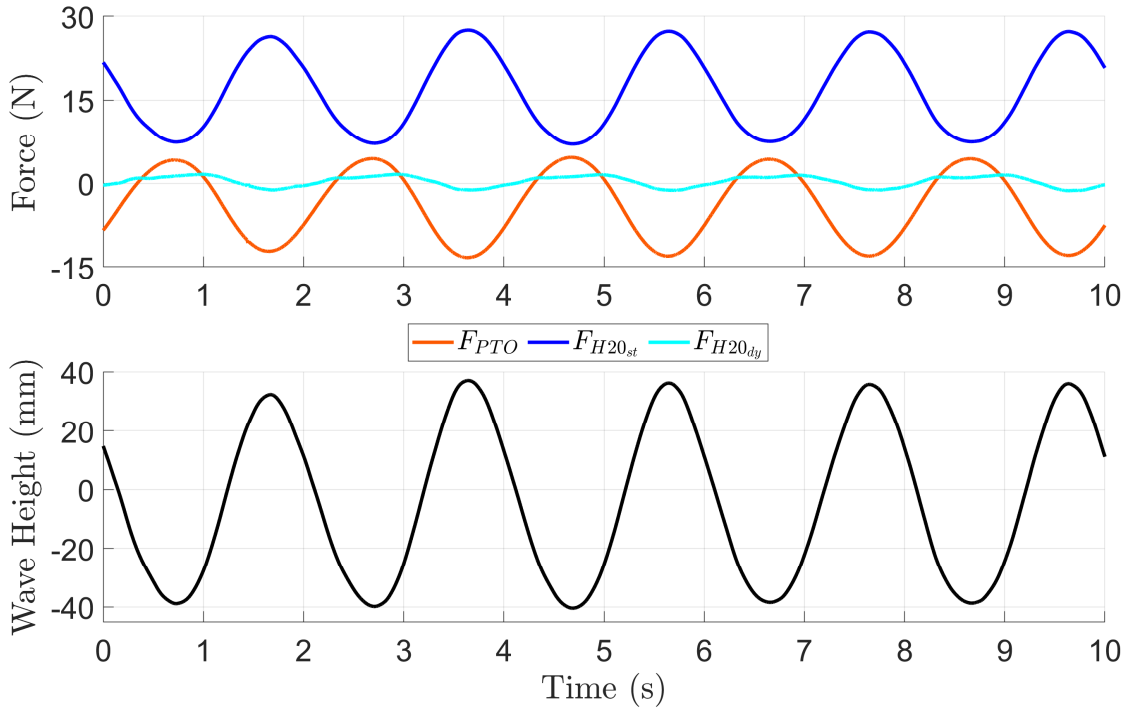

Figure 27: Stationary Buoy 40 mm Amplitude 0.5 Hz Frequency Trial

Examining the amplitude spectrum of the measured forces is still valuable despite the lack of noise, as it will allow for comparison with the spectrums produced by the noisy force data. Figure 28 presents the single-sided amplitude spectrum between 0 and 5 Hz of the measured F_{PTO} signal for the 40 mm amplitude, 0.5 Hz frequency trial.

Examining Figure 28 reveals large amplitude spikes at 0 and 0.5 Hz and negligible signal content at frequencies greater than 3 Hz. This result is consistent with the large DC component of the measured PTO force and the 0.5 Hz frequency of the incident waves. This result also further supports the use of a 5 Hz cutoff frequency for filtering the measured force data from the inertial force effects and moving buoy experiments, as it provides evidence that no meaningful signal content should be expected above the selected filter cutoff frequency.

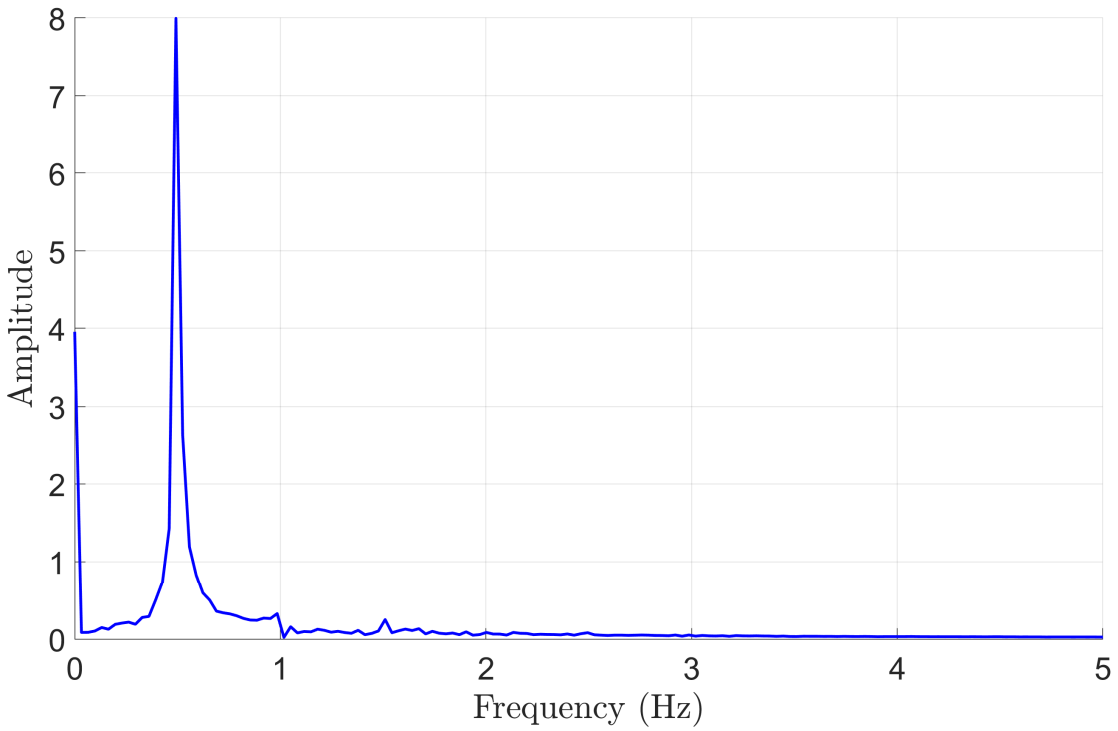

Figure 28: Single-Sided Amplitude Spectrum for Measured PTO Force from Stationary Buoy 40 mm Amplitude 0.5 Hz Frequency Trial

As was done for the moving buoy experiments, the maximum and average hydrodynamic force magnitude was calculated for all the experimental trials. These results are presented in Table 8. This was done to evaluate the measurability of these results with respect to the load cell error. No filtering was applied to the measured force data due to the lack of observable noise in the results.

Examining Table 8 shows a trend of increasing hydrodynamic force magnitudes with increases in wave amplitude. These results compare favorably to the load cell error, as all

the maximum and average hydrodynamic force magnitudes are greater than the maximum combined load cell error. However, the hydrodynamic force magnitudes are similar in size to the load cell error, limiting their practical utility.

Table 8: Maximum and Average Hydrodynamic Force Magnitudes for the Stationary Buoy Experiment

Experimental Trial	**Maximum Hydrodynamic Force Magnitude (N)**	**Average Hydrodynamic Force Magnitude (N)**
10 mm Amplitude, 1 Hz	1.184	0.612
20 mm Amplitude, 0.75 Hz	2.152	0.749
40 mm Amplitude, 0.5 Hz	2.605	0.926
50 mm Amplitude, 0.4 Hz	2.583	0.983

The hydrostatic and hydrodynamic forces for the first 10 seconds of each of the four experimental trials are plotted in Figures 29 and 30 respectively. Plotting the forces in this way allows for the relationship between the wave conditions and the force amplitudes to be evaluated visually.

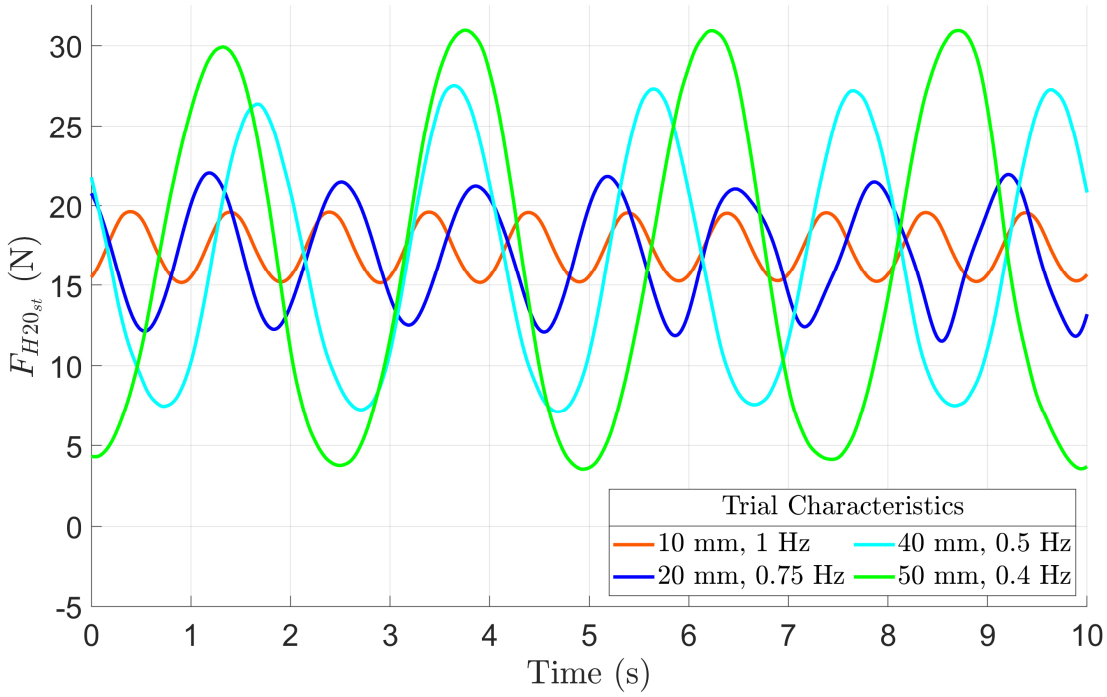

Figure 29: Stationary Buoy Experiment Hydrostatic Forces

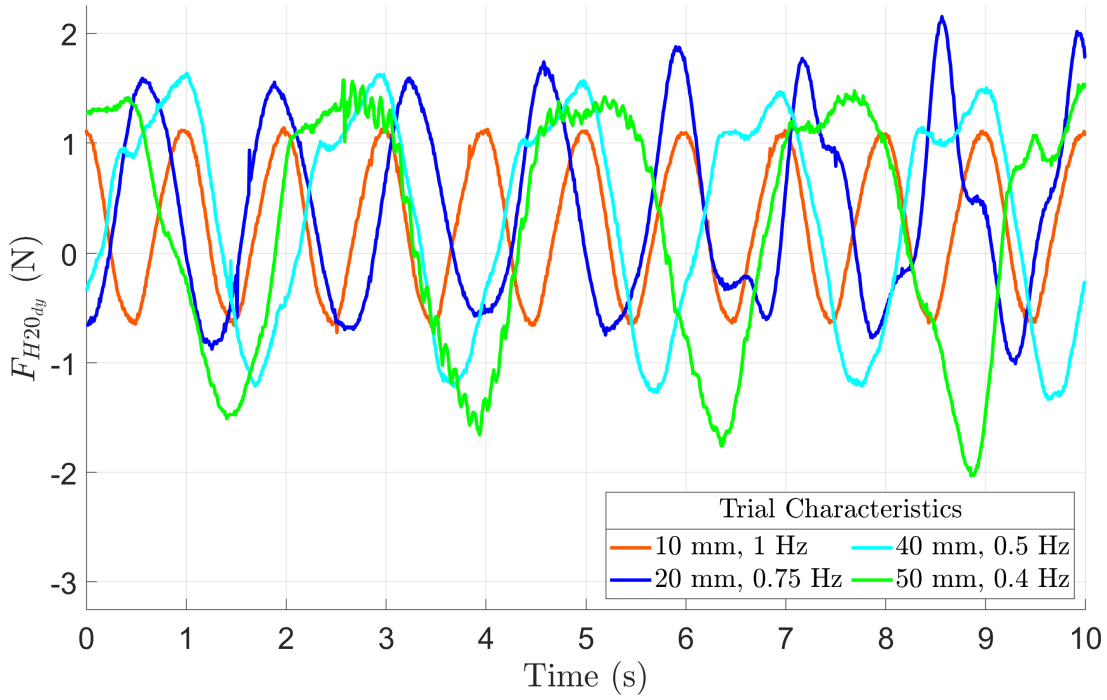

Figure 30: Stationary Buoy Experiment Hydrodynamic Forces

Figure 29 shows a strong relationship between the amplitude of the hydrostatic force and the height of the incident wave. This is expected, as larger waves submerge a greater volume of the buoy. In contrast, Figure 30 shows a much weaker relationship between the amplitude of the hydrodynamic force and the wave height, as the forces appear to have relatively similar amplitudes across all four experimental trials. This behavior can be better quantified by evaluating the force range for each experimental trial, as the range provides a convenient measure of amplitude. The hydrostatic and hydrodynamic force ranges and the static to dynamic ratio of the force ranges were calculated for each experimental trial. These results are presented in Table 9.

Table 9: Stationary Buoy Experiment Force Ranges and Ratios

Wave Amplitude (mm)	**Hydrostatic Force Range (N)**	**Hydrodynamic Force Range (N)**	**Static to Dynamic Force Ratio**
10	4.77	2.04	2.34
20	10.55	3.16	3.34
40	20.50	4.30	4.77
50	28.50	4.33	6.58

The results presented in Table 9 help quantify how the hydrostatic and hydrodynamic force amplitudes change with respect to the amplitude of the incident wave. The hydrostatic force range can be seen to increase dramatically with increasing wave amplitude while the hydrodynamic force range increases only marginally. The static to dynamic force ratio also increases with increased wave amplitude. This indicates that the hydrostatic force component is growing faster than the hydrodynamic as wave amplitude increases. These findings further support the observation made from Figures 29 and 30 that the hydrostatic force is more strongly influenced by the wave amplitude than the hydrodynamic force.

These results have some potentially interesting implications, as they suggest that the hydrodynamic force effects will be less significant relative to the hydrostatic force at larger wave amplitudes. However, it is worth noting that the four stationary buoy experimental trials all occurred at different wave frequencies in addition to different wave amplitudes. Experimental trials of different wave amplitudes at the same wave frequency would need to be conducted to decisively investigate the relationship between hydrodynamic force amplitude and wave height to ensure that the observed differences were only due to the wave amplitude and not the wave frequency.

This experiment has provided an example of how experimental hydrodynamic force determination could be performed using the force measuring device for a stationary test artifact in a wavefield. The results of this experiment are very promising, as the measured PTO force contained no observable noise and the determined hydrodynamic forces are large enough to verify that they are not the result of load cell error. Examining how the hydrostatic and hydrodynamic force amplitudes changed with respect to the wave amplitude yielded some interesting behavior that is worthy of further investigation. This experiment also made use relatively limited assumptions, as the wave height was measured using wave gauges and there were no inertial force effects to consider. However, the hydrodynamic forces obtained were similar in magnitude to the load cell error. Remedying this issue is expected to significantly improve the usefulness of these experimentally determined hydrodynamic forces for further research investigation.

4 Conclusions

This work has presented the development of a custom device capable of measuring the vertical forces exerted on a test artifact in a laboratory wave tank and has demonstrated methods for determining the hydrodynamic force component from measured force data. Conclusions regarding the device effectiveness, recommended improvements to the device and analysis methods, and future work are presented in the following subsections.

4.1 Summary of Device Effectiveness

The device was shown to serve its intended purpose through experiments validating its force measuring capabilities and demonstrating hydrodynamic force determination. The design of the load cell subassembly was found to protect the load cell from side loading without significantly distorting the measured forces. The proposed hydrodynamic force determination technique was implemented during demonstrative experiments and used to successfully obtain hydrodynamic forces large enough to be measured by the device. The stationary buoy in a wavefield experiment experienced the most successful outcome, as this experiment used the fewest assumptions and produced the cleanest results.

However, the device and the presented hydrodynamic force determination technique have limitations and shortcomings that require resolution before the device can be effectively used to its fullest potential. The forces measured during the experiments involving buoy motion contained significant noise that is hypothesized to be the result of vibrations experienced by the device's truss structure. The technique used to calculate the inertial force effects was found to produce significant error, most likely due to the assumptions made while determining the acceleration of the test artifact. The moving buoy in calm water experiment utilized this method while determining the hydrodynamic forces, making the results of this experiment of limited value beyond demonstration. The stationary buoy experiment did not use this technique, as the buoy acceleration was known to be zero. The hydrodynamic forces determined during both the moving and stationary buoy experiments were similar in magnitude to the maximum combined error of the load cell. This limits the additional usefulness of the hydrodynamic force results obtained during these experiments.

4.2 Recommended Improvements

Improvements to resolve the limitations and shortcomings of the force measuring device and hydrodynamic force determination technique are necessary to maximize the experimental capabilities provided by the device. The stability of the truss structure can be improved using brackets to attach the truss to the walkway that spans the width of the MTU wave tank. This will help reduce the vibrations experienced by the truss and the noise in the measured forces during experiments involving test artifact motion. The position of the test artifact can be measured directly instead of being obtained from the actuator position command. This will eliminate one of the assumptions that was used to determine the hydrodynamic force and is expected to produce more accurate results. This can be done using the actuator itself or the MTU Wave Tank Laboratory's motion capture camera system. The acceleration used to calculate the inertial force effects can be measured directly using an accelerometer instead of being derived from the test artifact position. This will eliminate the errors that result from determining the acceleration using finite differencing differentiation. Alternatively, acceleration can also be determined by applying the same finite differencing differentiation method to the measured test artifact position instead of the actuator position command. This is expected to produce more accurate acceleration values than those obtained during this project by eliminating the perfect actuator tracking assumption. Wave gauges can be used during experiments involving buoy motion to eliminate the calm water surface assumption that was used to determine the hydrostatic force. This will also make it possible to do experiments with a moving buoy in a wavefield. A larger test artifact (to produce larger forces) and/or a load cell with a smaller maximum error can be used to ensure that the hydrodynamic forces can be determined with a high level of accuracy and precision relative to their magnitude.

4.3 Future Work

Additional stationary buoy experiments further exploring the relationship between the hydrodynamic force amplitude and the wave amplitude are a priority due to the interesting preliminary results obtained during this project and the potential implications of these results. Further validation of the device can be performed by comparing the hydrodynamic forces determined using the device to a validated CFD model. Strong agreement between

these two approaches will ensure a high level of confidence in the results produced by both methods. Experimentally determined hydrodynamic forces obtained using the device can be used to experimentally validate theoretical models and develop data-based force prediction methods. The device can also be modified to add new functionality, such as the addition of a multi-axis load cell to investigate force vectors instead of one-dimensional force components. The work presented in this report provides the foundation necessary to pursue these and many other related research questions using experimental techniques.

5 References

[1] A. Clément *et al.*, "Wave energy in Europe: current status and perspectives," *Renewable and sustainable energy reviews,* vol. 6, no. 5, pp. 405-431, 2002.

[2] K. Gunn and C. Stock-Williams, "Quantifying the potential global market for wave power," in *Proceedings of the 4th International Conference on Ocean Engineering (ICOE 2012)*, 2012, pp. 1-7.

[3] S. Astariz and G. Iglesias, "The economics of wave energy: A review," *Renewable and Sustainable Energy Reviews,* vol. 45, pp. 397-408, 2015, doi: 10.1016/j.rser.2015.01.061.

[4] U. A. Korde, "Control system applications in wave energy conversion," IEEE, doi: 10.1109/oceans.2000.882202. [Online]. Available: https://dx.doi.org/10.1109/oceans.2000.882202

[5] G. Giorgi and J. V. Ringwood, "Analytical representation of nonlinear Froude-Krylov forces for 3-DoF point absorbing wave energy devices," *Ocean Engineering,* vol. 164, pp. 749-759, 2018.

[6] G. Giorgi and J. V. Ringwood, "Computationally efficient nonlinear Froude–Krylov force calculations for heaving axisymmetric wave energy point absorbers," *Journal of Ocean Engineering and Marine Energy,* vol. 3, no. 1, pp. 21-33, 2017.

[7] G. Giorgi and J. V. Ringwood, "Nonlinear Froude-Krylov and viscous drag representations for wave energy converters in the computation/fidelity continuum," *Ocean Engineering,* vol. 141, pp. 164-175, 2017.

[8] G. Giorgi, S. Sirigu, M. Bonfanti, G. Bracco, and G. Mattiazzo, "Fast nonlinear Froude–Krylov force calculation for prismatic floating platforms: a wave energy conversion application case," *Journal of Ocean Engineering and Marine Energy,* vol. 7, no. 4, pp. 439-457, 2021, doi: 10.1007/s40722-021-00212-z.

[9] M. Penalba, G. Giorgi, and J. V. Ringwood, "Mathematical modelling of wave energy converters: A review of nonlinear approaches," *Renewable and Sustainable Energy Reviews,* vol. 78, pp. 1188-1207, 2017.

[10] D. Evans, D. Jeffrey, S. Salter, and J. Taylor, "Submerged cylinder wave energy device: theory and experiment," *Applied Ocean Research,* vol. 1, no. 1, pp. 3-12, 1979.

[11] H.-N. Nguyen and P. Tona, "Wave excitation force estimation for wave energy converters of the point-absorber type," *IEEE Transactions on Control Systems Technology,* vol. 26, no. 6, pp. 2173-2181, 2017.

[12] A. S. Zurkinden, F. Ferri, S. Beatty, J. P. Kofoed, and M. M. Kramer, "Non-linear numerical modeling and experimental testing of a point absorber wave energy converter," *Ocean Engineering,* vol. 78, pp. 11-21, 2014, doi: 10.1016/j.oceaneng.2013.12.009.

[13] S. J. Beatty, B. Bocking, K. Bubbar, B. J. Buckham, and P. Wild, "Experimental and numerical comparisons of self-reacting point absorber wave energy converters in irregular waves," *Ocean Engineering,* vol. 173, pp. 716-731, 2019.

[14] S. J. Beatty, M. Hall, B. J. Buckham, P. Wild, and B. Bocking, "Experimental and numerical comparisons of self-reacting point absorber wave energy converters in regular waves," *Ocean Engineering,* vol. 104, pp. 370-386, 2015, doi: 10.1016/j.oceaneng.2015.05.027.

[15] E. Mackay, J. Cruz, C. Retzler, P. Arnold, E. Bannon, and R. Pascal, "Validation of a new wave energy converter design tool with large scale single machine experiments," in *1st Asian wave and tidal conference series*, 2012.

[16] G. Giorgi, R. P. Gomes, J. C. Henriques, L. M. Gato, G. Bracco, and G. Mattiazzo, "Detecting parametric resonance in a floating oscillating water column device for wave energy conversion: Numerical simulations and validation with physical model tests," *Applied Energy,* vol. 276, p. 115421, 2020.

[17] B. Guo, R. J. Patton, S. Jin, and J. Lan, "Numerical and experimental studies of excitation force approximation for wave energy conversion," *Renewable energy,* vol. 125, pp. 877-889, 2018.

[18] X. L. Zhao, D. Z. Ning, and D. F. Liang, "Experimental investigation on hydrodynamic performance of a breakwater-integrated WEC system," *Ocean Engineering,* vol. 171, pp. 25-32, 2019, doi: 10.1016/j.oceaneng.2018.10.036.

[19] G. Giorgi, M. Penalba, and J. Ringwood, "Nonlinear hydrodynamic force relevance for heaving point absorbers and oscillating surge converters," 2016.

[20] D. R. Noble, S. Draycott, T. A. D. Davey, and T. Bruce, "Design diagrams for wavelength discrepancy in tank testing with inconsistently scaled intermediate water depth," *International Journal of Marine Energy,* vol. 18, pp. 109-113, 2017, doi: 10.1016/j.ijome.2017.04.001.

[21] D. A. Winter, *Biomechanics and motor control of human movement*. John Wiley & Sons, 2009.

[22] S. G. Swartzmiller, "Development of a fused deposition 3D printed buoy and method for quantifying wave tank reflections," Michigan Technological University, 2019.

A Force Measuring Device Design

A.1 Summary of Device Component Specifications

Table A-1: Selected Load Cell Specifications

Specification Description	Specification Value
Manufacturer	Sensing Systems Corporation
Full Scale Capacity (FS)	+/- 50 lbf (222 N)
Safe Overload	150% of FS
Ultimate Overload	300% of FS
Combined Error	$\leq 0.250\%$ of FS
Calibration	NIST Traceable per ASTM E4
Material	Anodized Aluminum
Operating Depth	$\leq$ 10 ft (3.05 m)

Table A-2: Selected Linear Actuator Specifications

Specification Description	Specification Value
Manufacturer	Ultra Motion
Product Series	Industrial – Series A2
Peak Force	180 lbf (800 N)
Max Speed (Unloaded)	15 in/s (25.4 mm/s)
Motor	100 Watt BLDC
Operating Voltage	36 VDC
Actuator Travel (Stroke)	7.75 in (0.197 m)
Environment Protection Rating	IP65

Table A-3: Selected Load Cell Shaft and Bearing Specifications

Specification Description	Specification Value
Manufacturer	Thomson
Bearing Part Number	SSU10-CR
Ball Bearing Material	440C Stainless Steel
Bearing Plate Finish	Hard Chrome-Plated
Bearing Coefficient of Static Friction	≤ 0.0040
Bearing Dynamic Load Capacity	620 lbf (2758 N)
Shaft Diameter	0.625 in (15.875 mm)
Shaft Material	440C Stainless Steel

Table A-4: Selected Spar and Spar Bearing Specifications

Specification Description	Specification Value
Supplier	McMaster-Carr
Bearing Part Number	60255K54
Static Load Capacity	1800 lbf (8007 N)
Static Pitch Moment Load Capacity	110 ft-lbf (149.14 N-m)
Static Roll Moment Load Capacity	34 ft-lbf (46.10 N-m)
Static Yaw Moment Load Capacity	110 ft-lbf (149.14 N-m)
Bearing Carriage Material	Aluminum
Bearing Plug Material	316 Stainless Steel
Bearing Pad Material	Frelon Plastic
Spar Material	304 Stainless Steel

A.2 List of Custom Components

Table A-5: Device Custom Components List

Part Name	Quantity	Part Material
Left Bearing Bracket	1	6061 Aluminum
Right Bearing Bracket	1	6061 Aluminum
Actuator Mount Plate	1	303 Stainless Steel
Spar Plug	2	303 Stainless Steel
Top Cylinder Linkage	1	6061 Aluminum
Back Bearing Bracket	2	6061 Aluminum
Hinge Mount	1	303 Stainless Steel
Clevis Bracket	2	6061 Aluminum
Spacer Plate	1	6061 Aluminum
Caster Mount	4	303 Stainless Steel
Load Cell Amp Mount	1	6061 Aluminum
Handle Mount Plate	2	6061 Aluminum
Top Load Cell Support	1	303 Stainless Steel
Bottom Load Cell Support	1	303 Stainless Steel
Side Load Cell Support with Handle	1	303 Stainless Steel
Side Load Cell Support with Dowels	1	303 Stainless Steel
Spar	1	304 Stainless Steel

A.3 Purchasing List

The full list of the purchased materials used to fabricate the device is available at the following link:

https://docs.google.com/spreadsheets/d/1Vw2TYl2lRz29zqu0T10sJNWsKL4x8Il7/edit?usp=sharing&ouid=108239036919538473198&rtpof=true&sd=true

A.4 Part Drawings

The drawing package for the custom parts used to fabricate the device is available at the following link:

https://drive.google.com/file/d/18rCh_VrzkzsbyaixRnTYreLdncEaztxq/view?usp=sharing

A.5 CAD Models

The CAD models of the device design can be found at the following link:

https://drive.google.com/drive/folders/1PgVogDn_QRU3VzOVQcLkbOqd69yQL4Qq?usp=sharing

B MATLAB Code and Experiment Data

The MATLAB code used to analyze the experiment data and the raw data obtained from the experiments described in this report can be found at the following link:

https://drive.google.com/drive/folders/1Mw6tcuWnQ83t-c0jivAUhCF9pajIgmms?usp=sharing

C Results Plots for All Experimental Trials

C.1 Inertial Force Effects Experiment

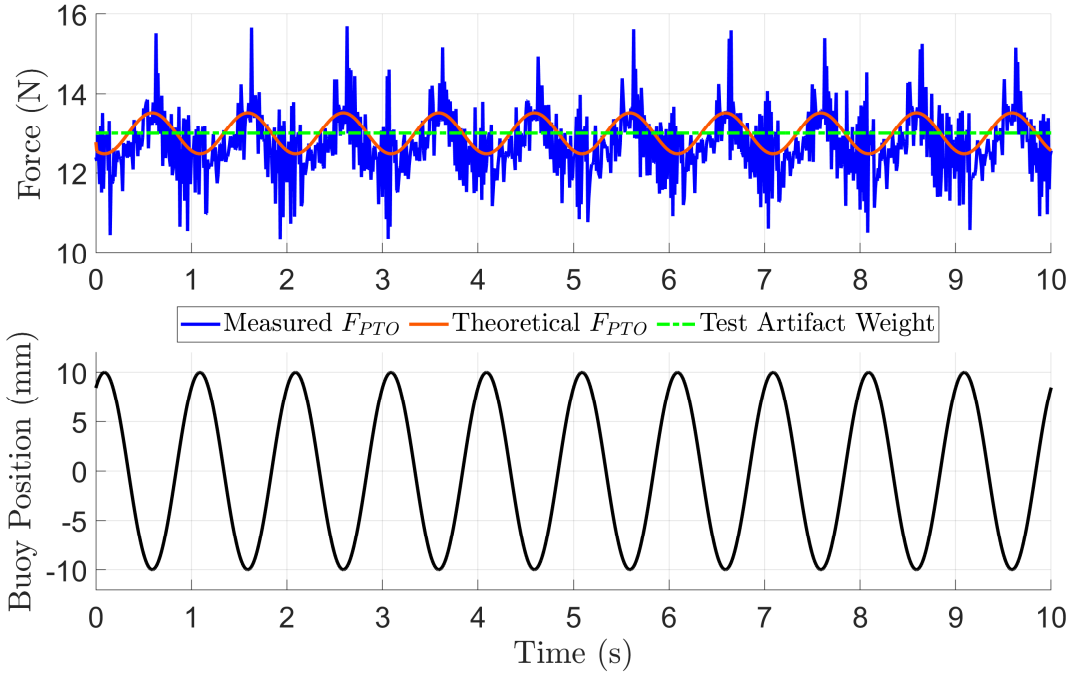

Figure C-1: Inertial Force Effects 10 mm Amplitude 1 Hz Frequency Trial

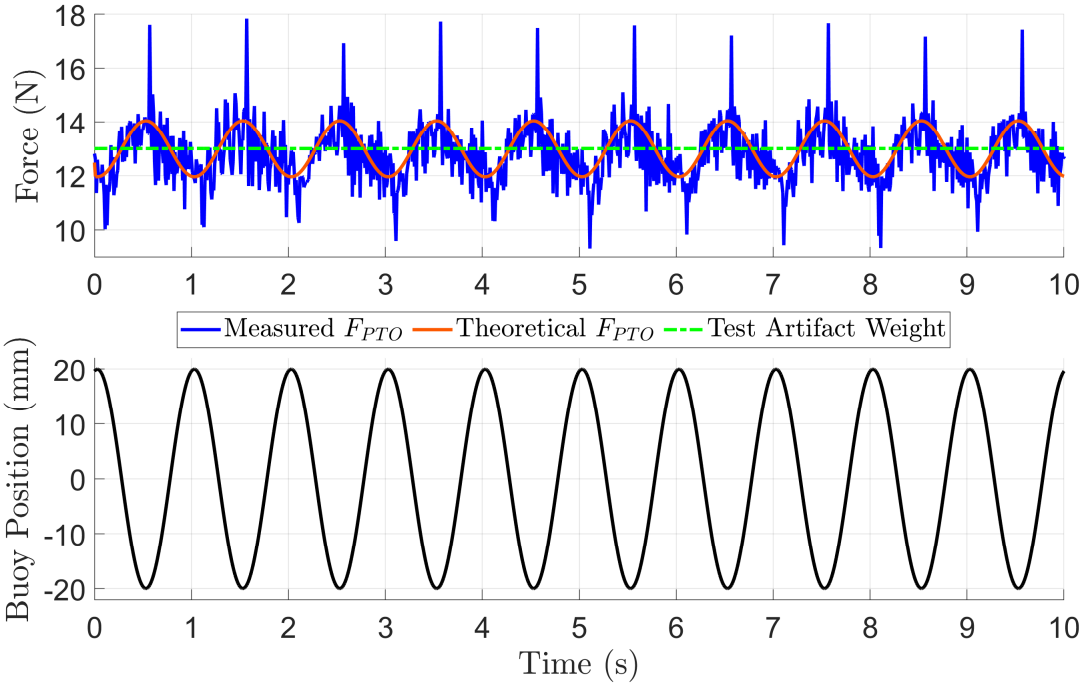

Figure C-2: Inertial Force Effects 20 mm Amplitude 1 Hz Frequency Trial

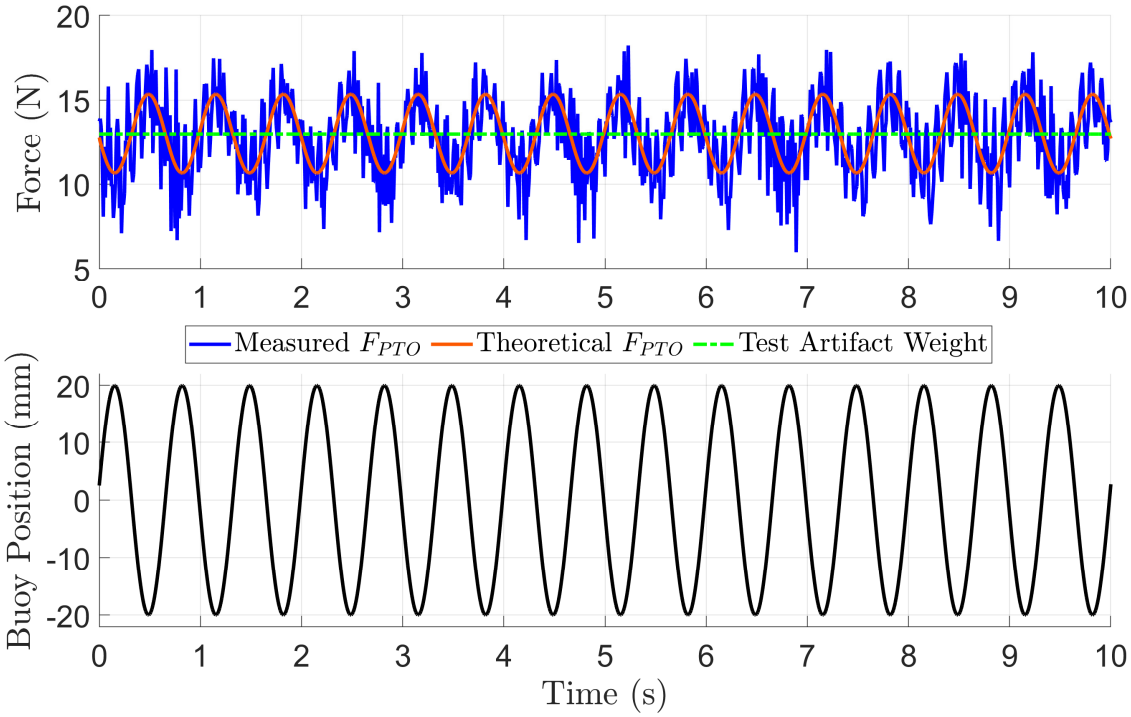

Figure C-3: Inertial Force Effects 20 mm Amplitude 1.5 Hz Frequency Trial

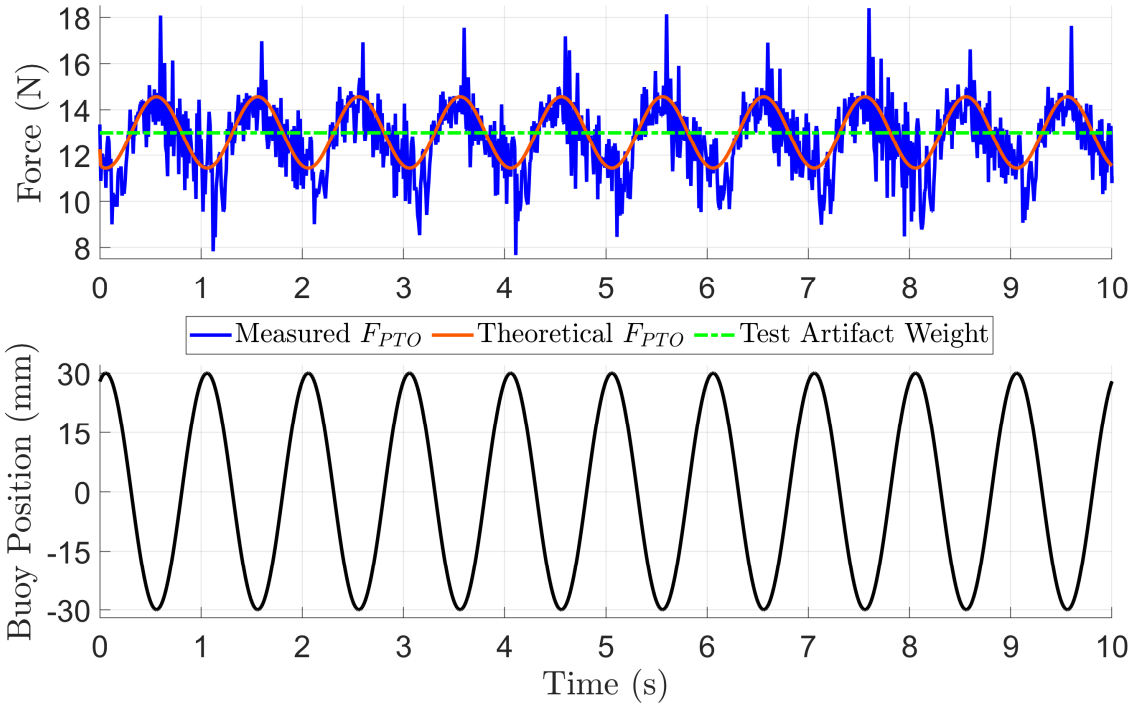

Figure C-4: Inertial Force Effects 30 mm Amplitude 1 Hz Frequency Trial

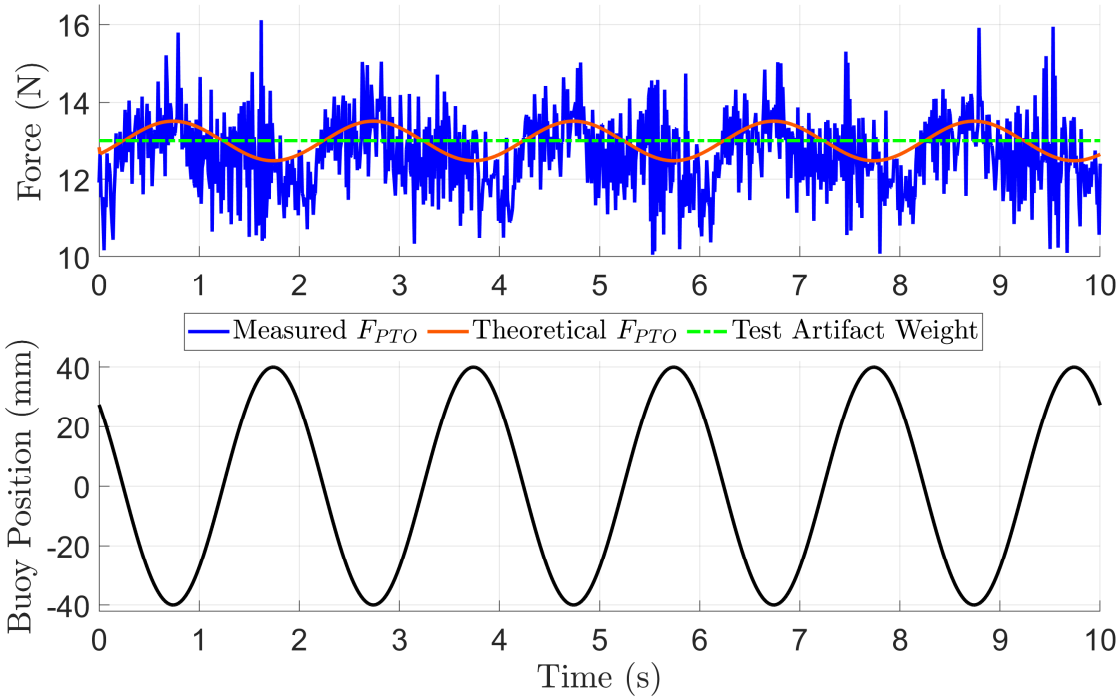

Figure C-5: Inertial Force Effects 40 mm Amplitude 0.5 Hz Frequency Trial

C.2 Moving Buoy Experiment in Calm Water

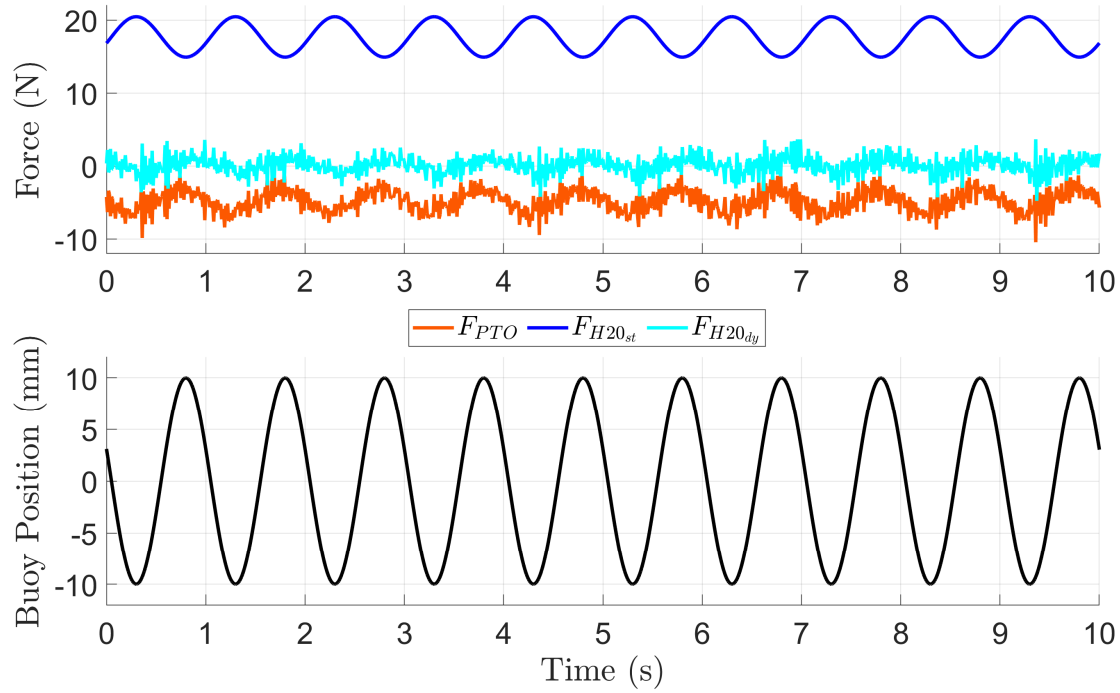

Figure C-6: Moving Buoy 10 mm Amplitude 1 Hz Frequency Trial

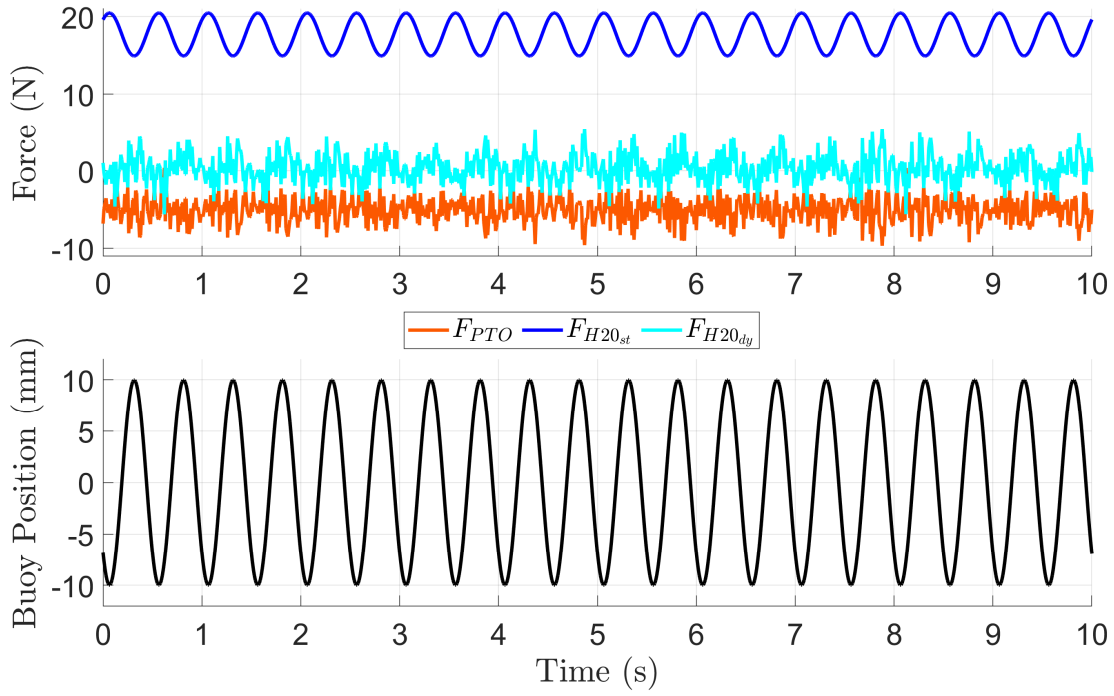

Figure C-7: Moving Buoy 10 mm Amplitude 2 Hz Frequency Trial

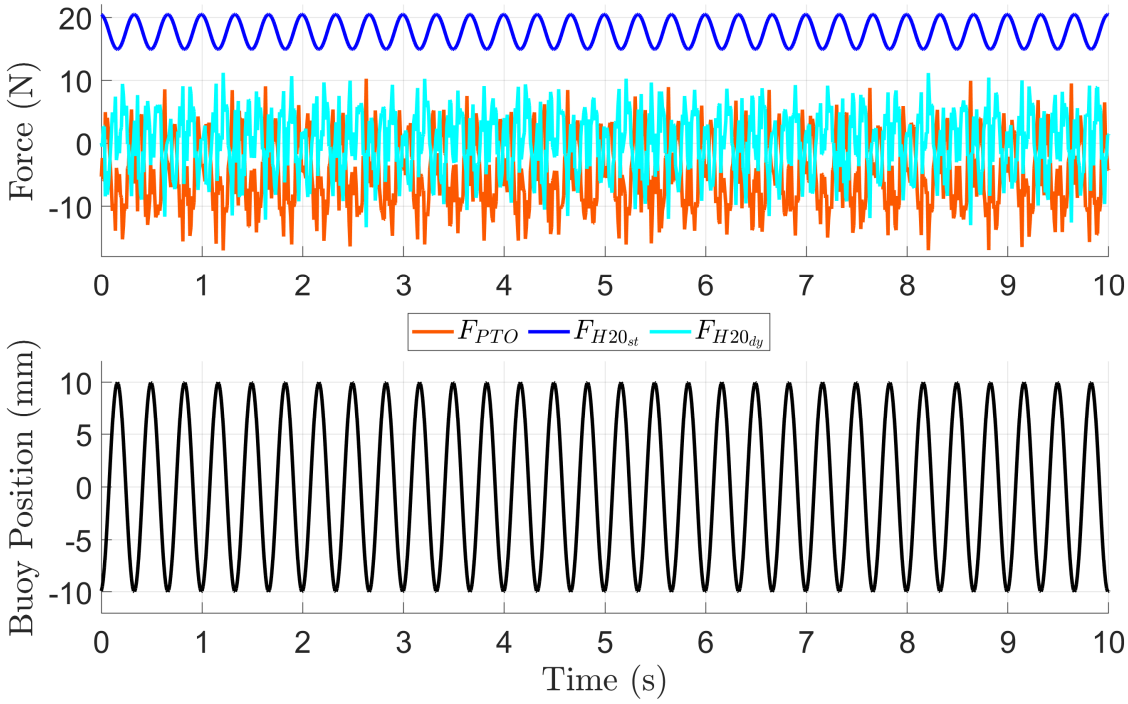

Figure C-8: Moving Buoy 10 mm Amplitude 3 Hz Frequency Trial

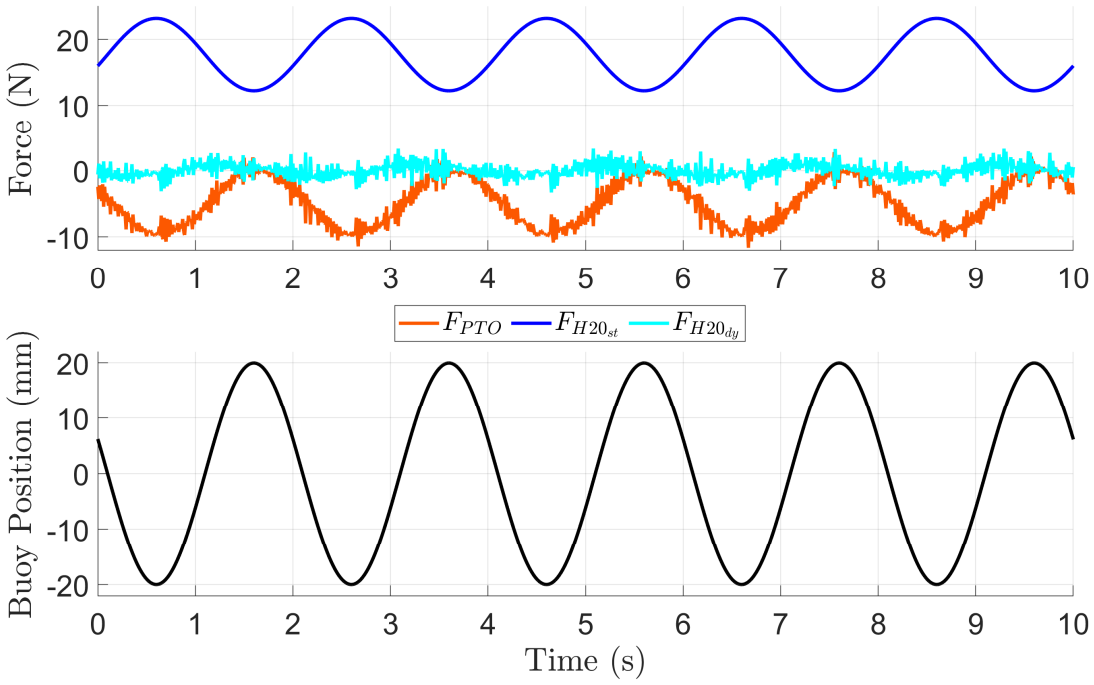

Figure C-9: Moving Buoy 20 mm Amplitude 0.5 Hz Frequency Trial

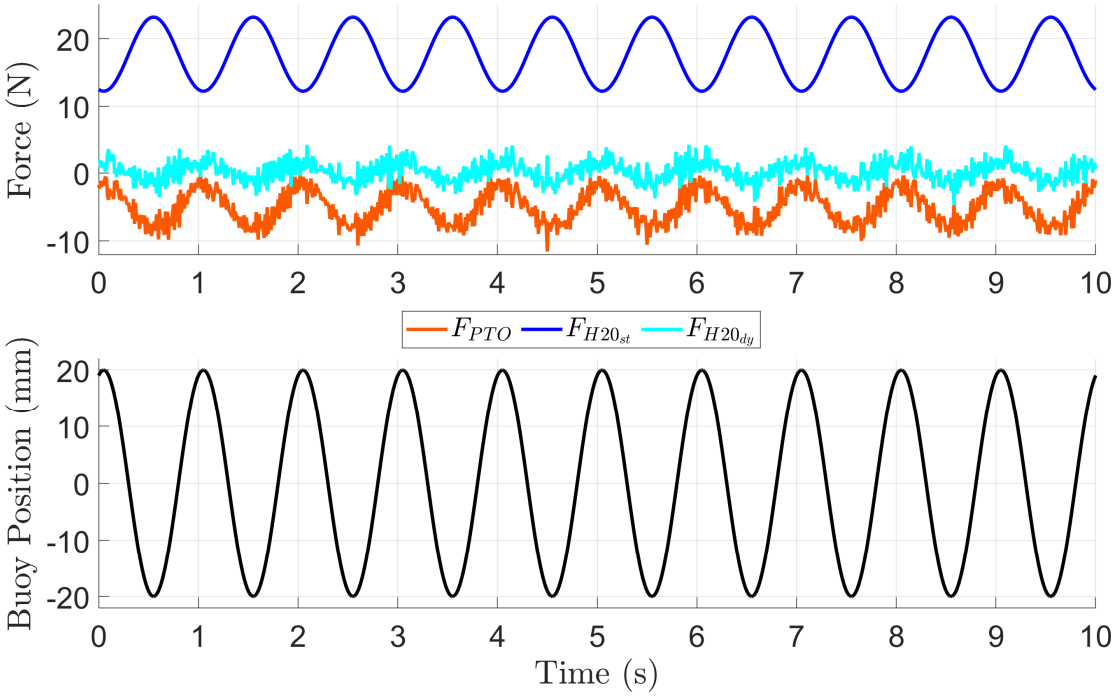

Figure C-10: Moving Buoy 20 mm Amplitude 1 Hz Frequency Trial

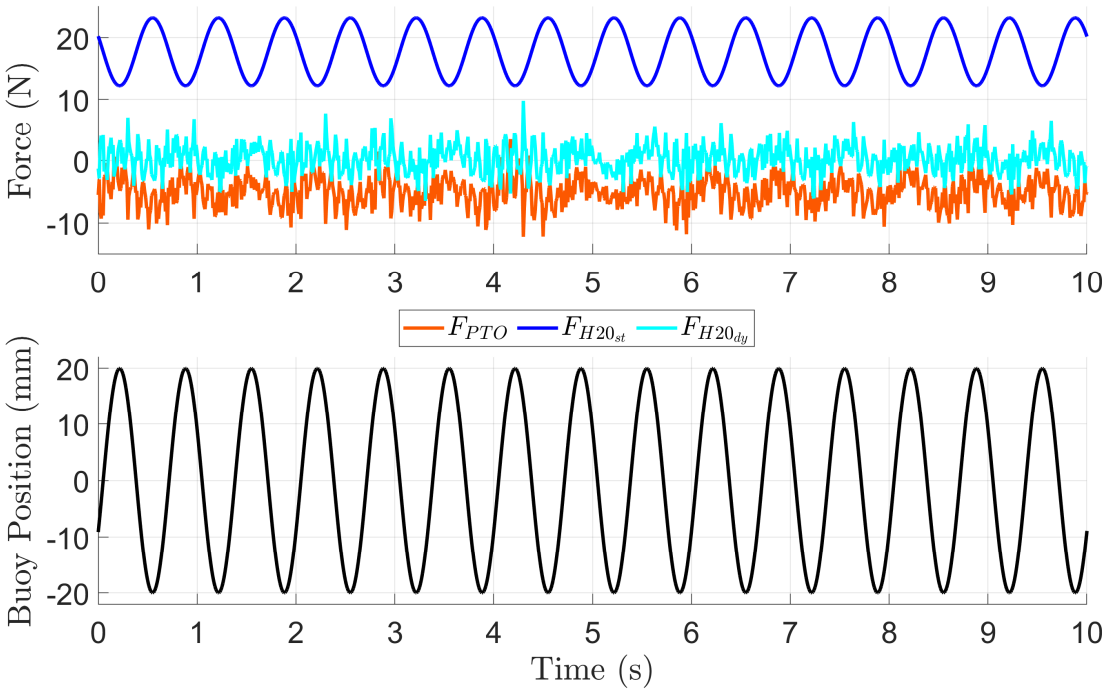

Figure C-11: Moving Buoy 20 mm Amplitude 1.5 Hz Frequency Trial

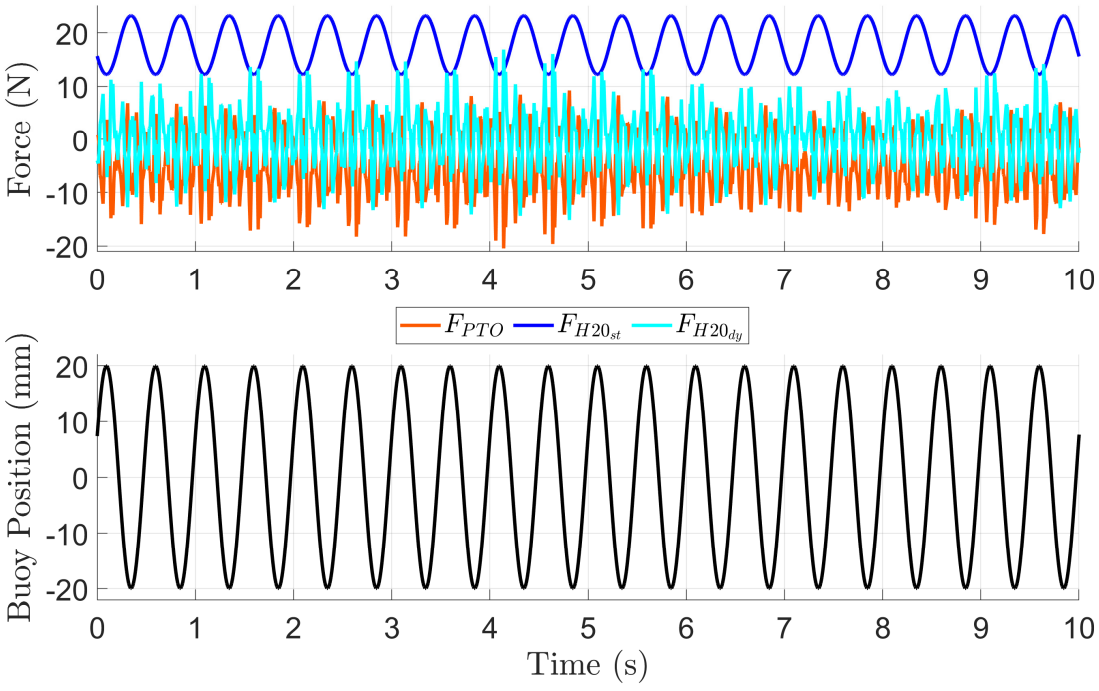

Figure C-12: Moving Buoy 20 mm Amplitude 2 Hz Frequency Trial

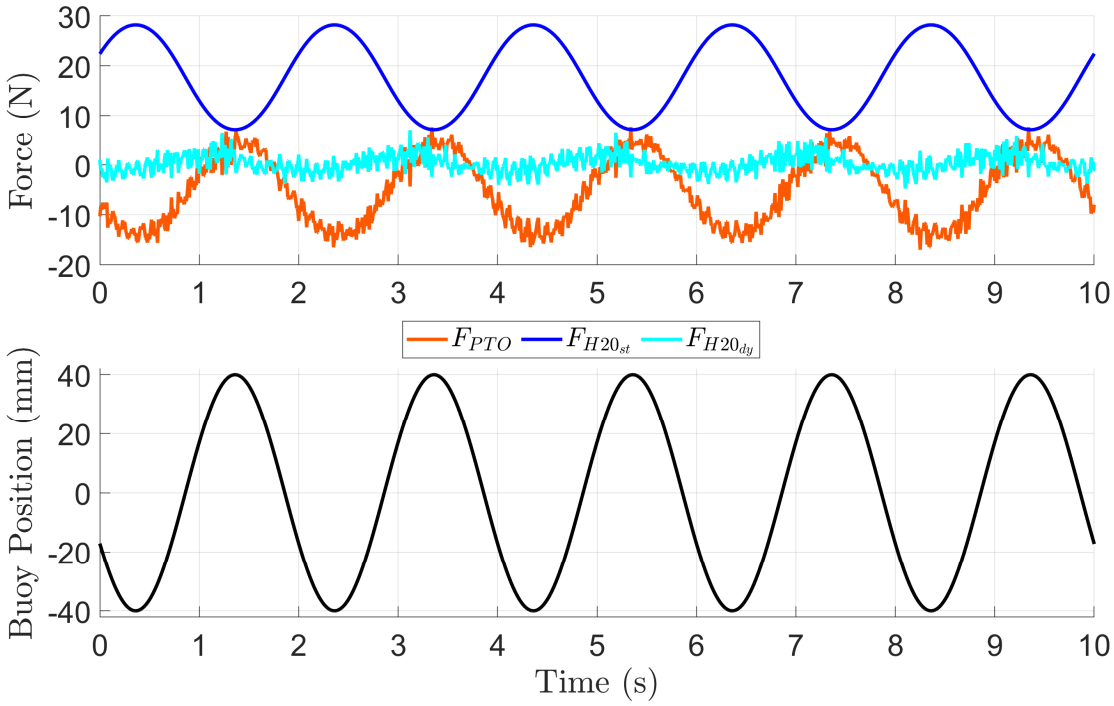

Figure C-13: Moving Buoy 40 mm Amplitude 0.5 Hz Frequency Trial

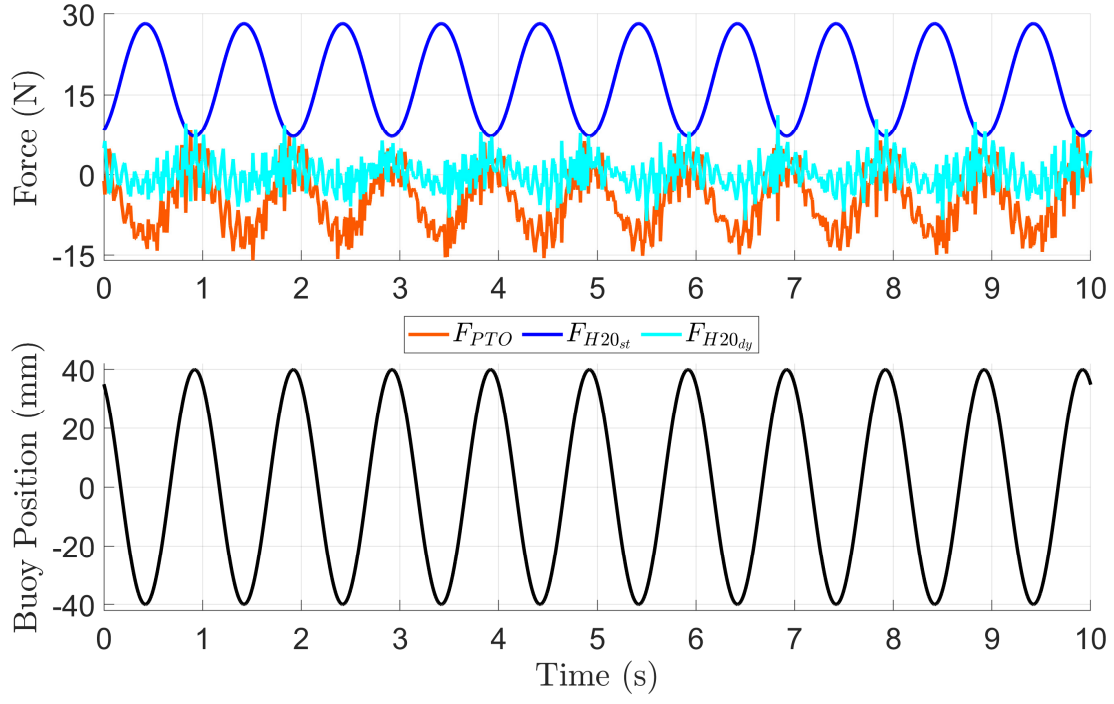

Figure C-14: Moving Buoy 40 mm Amplitude 1 Hz Frequency Trial

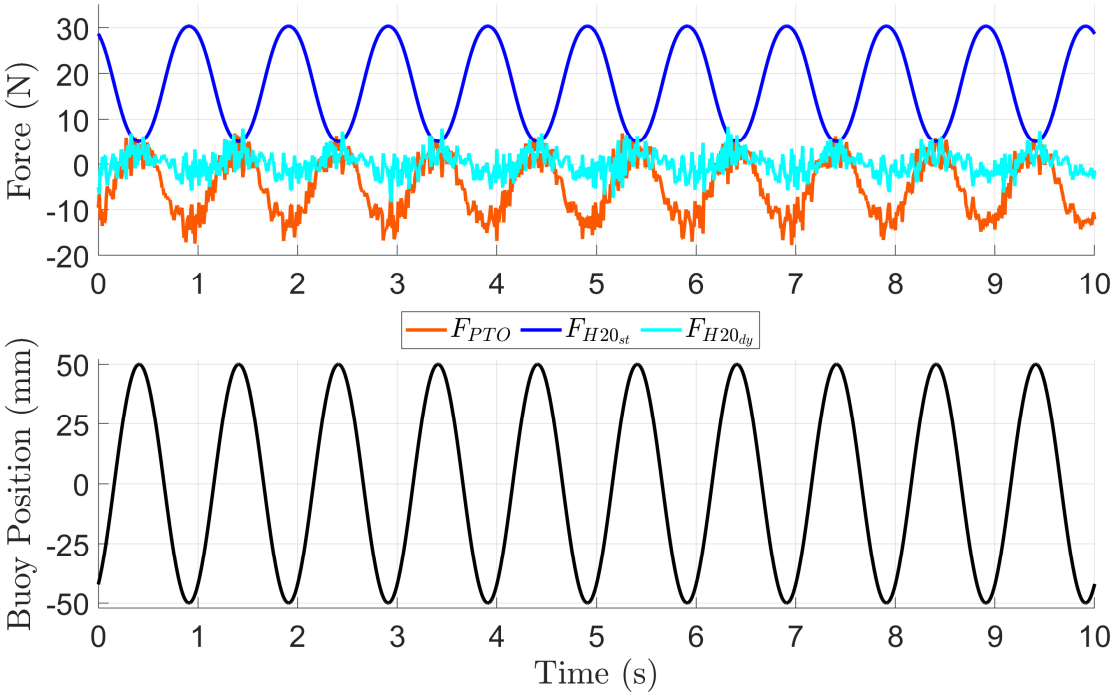

Figure C-15: Moving Buoy 50 mm Amplitude 1 Hz Frequency Trial

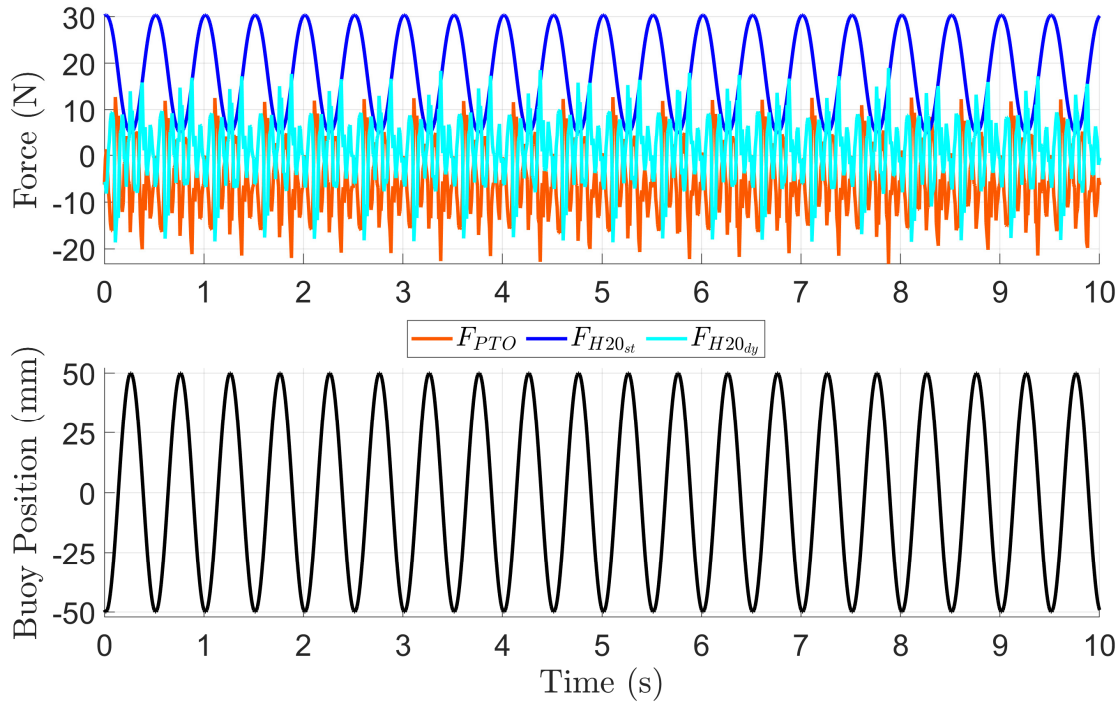

Figure C-16: Moving Buoy 50 mm Amplitude 2 Hz Frequency Trial

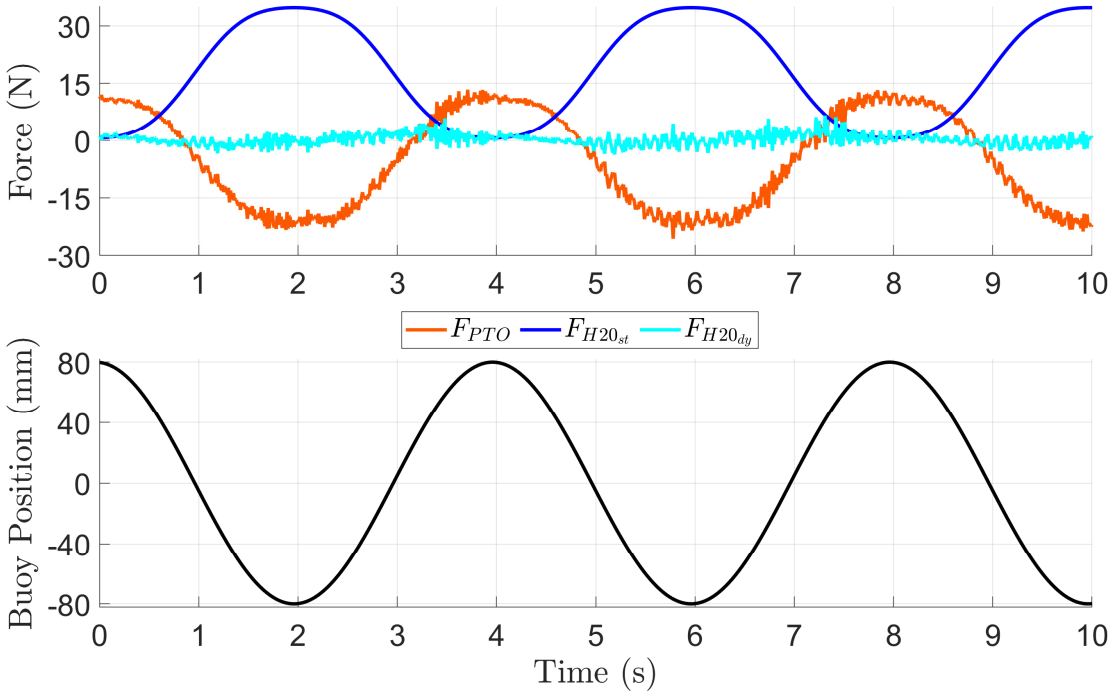

Figure C-17: Moving Buoy 80 mm Amplitude 0.25 Hz Frequency Trial

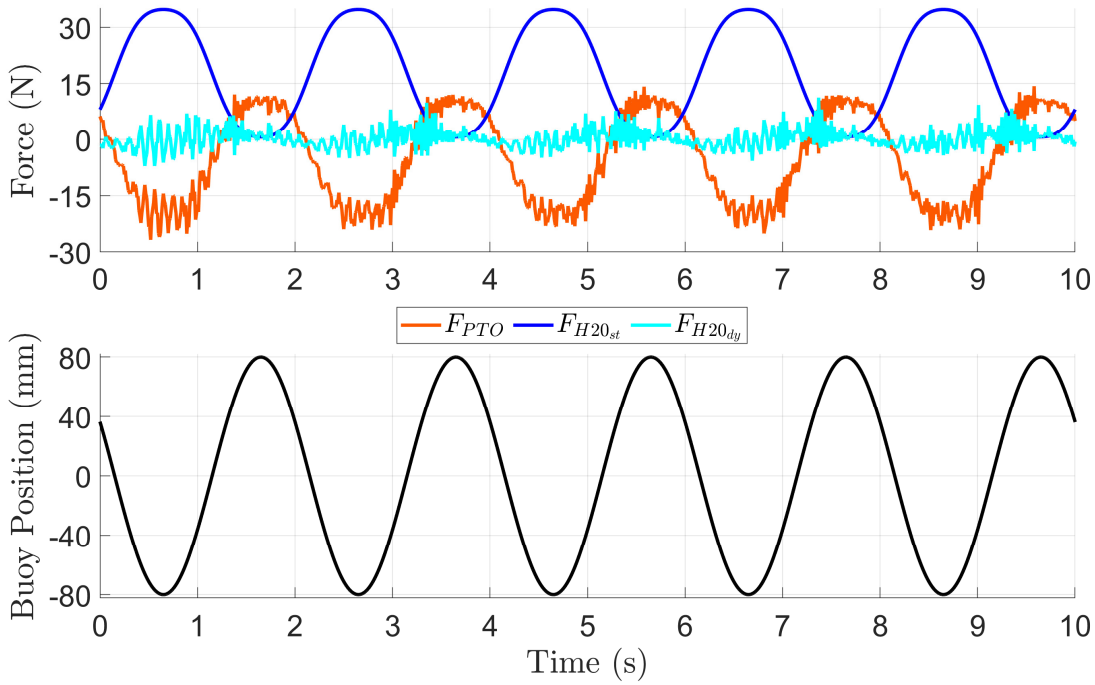

Figure C-18: Moving Buoy 80 mm Amplitude 0.5 Hz Frequency Trial

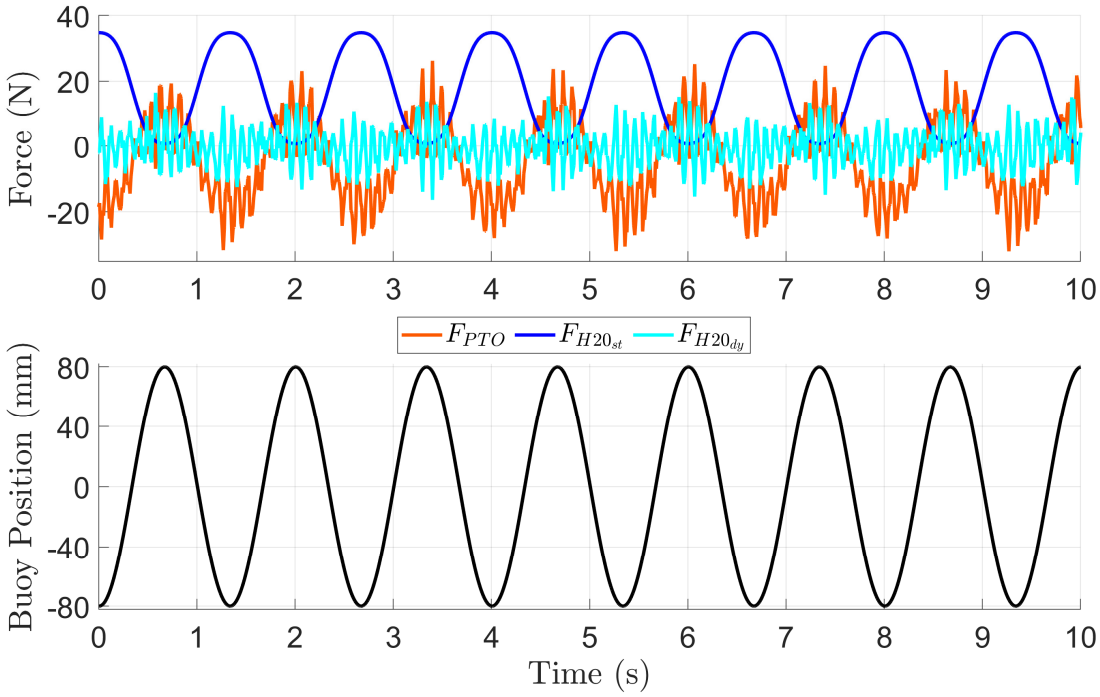

Figure C-19: Moving Buoy 80 mm Amplitude 0.75 Hz Frequency Trial

C.3 Stationary Buoy Experiment in a Wavefield

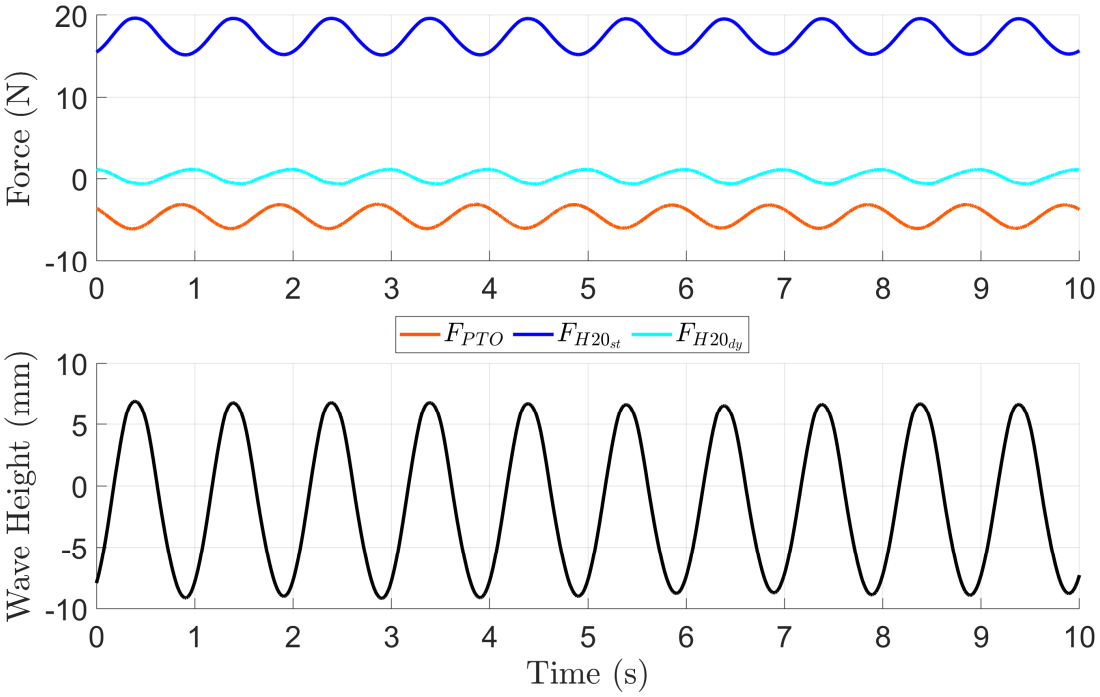

Figure C-20: Stationary Buoy 10 mm Amplitude 1 Hz Frequency Trial

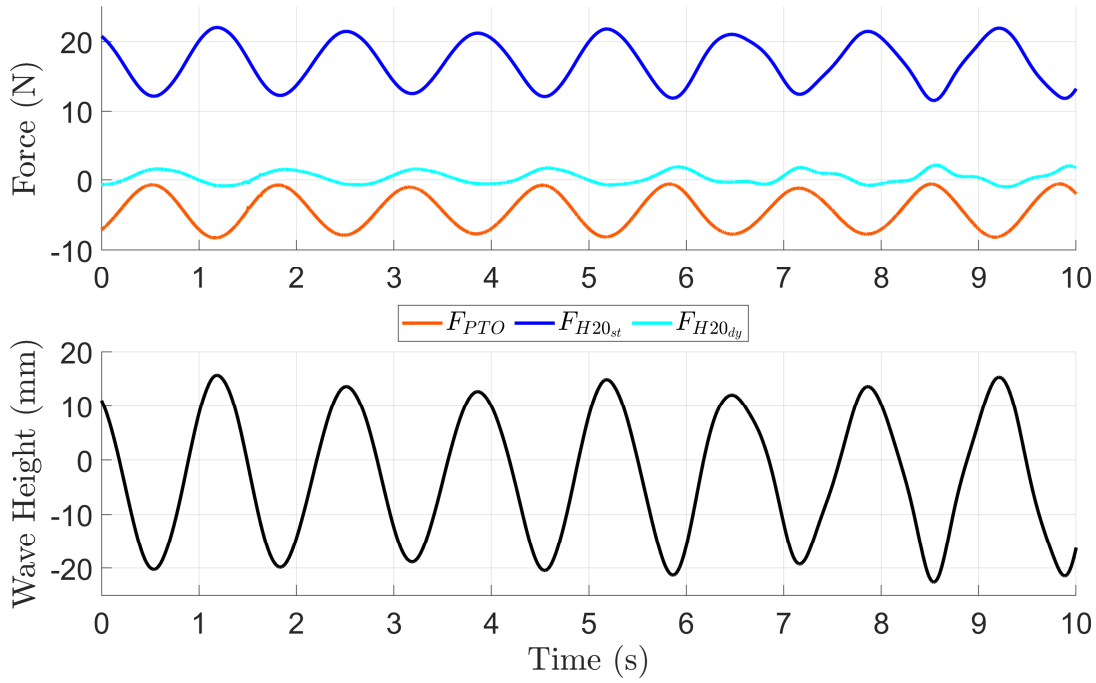

Figure C-21: Stationary Buoy 20 mm Amplitude 0.75 Hz Frequency Trial

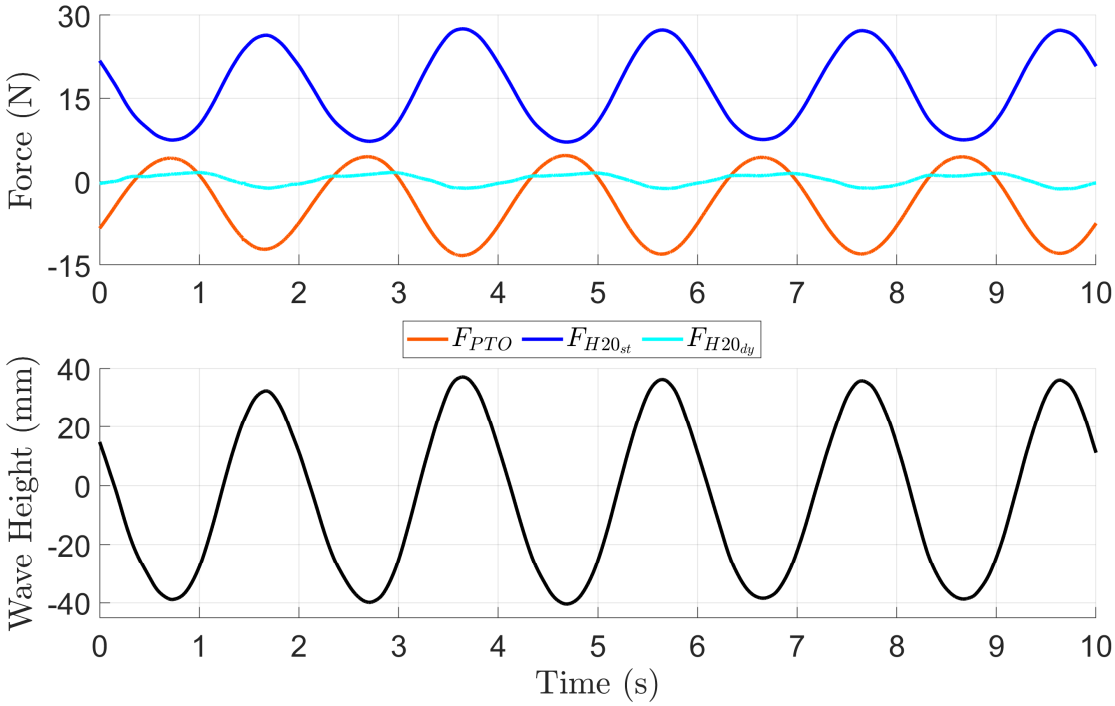

Figure C-22: Stationary Buoy 40 mm Amplitude 0.5 Hz Frequency Trial

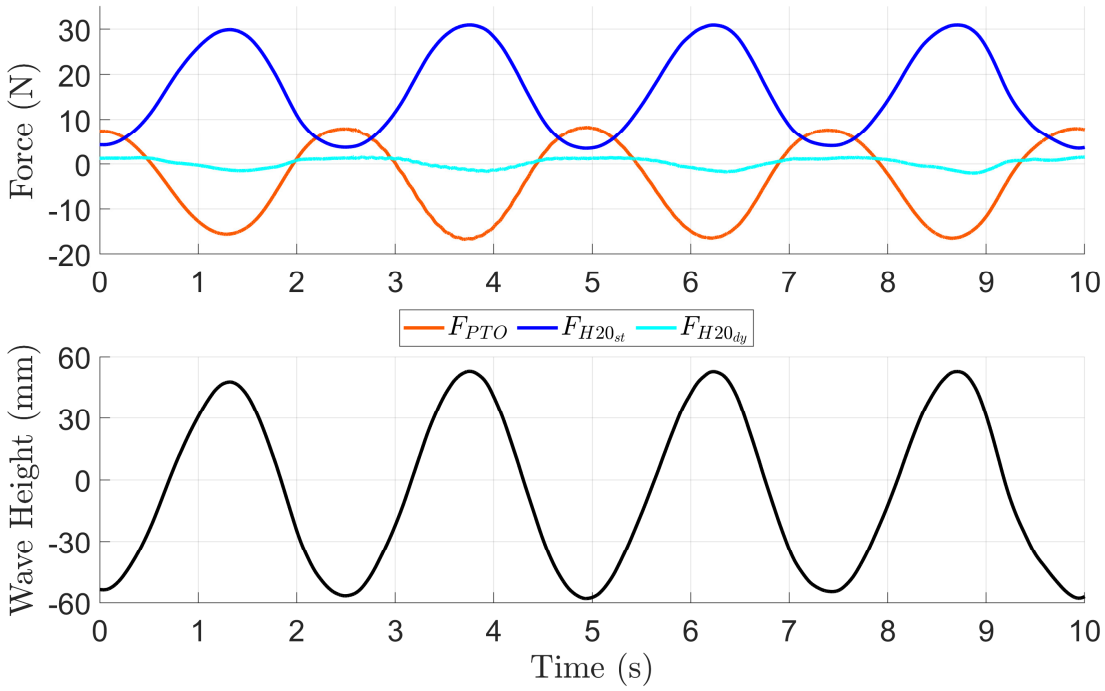

Figure C-23: Stationary Buoy 50 mm Amplitude 0.4 Hz Frequency Trial